Human Molecular Genetics, 2013, Vol. 22, No. 10 **2067–2082**
doi:10.1093/hmg/ddt057
Advance Access published on February 7, 2013

Atp13a2-deficient mice exhibit neuronal ceroid lipofuscinosis, limited α-synuclein accumulation and age-dependent sensorimotor deficits

Patrick J. Schultheis[1,*], Sheila M. Fleming[3], Amy K. Clippinger[1], Jada Lewis[5], Taiji Tsunemi[7,8], Benoit Giasson[5], Dennis W. Dickson[6], Joseph R. Mazzulli[7,8], Mark E. Bardgett[2], Kristi L. Haik[1], Osunde Ekhator[3], Anil Kumar Chava[1], John Howard[5], Matt Gannon[2], Elizabeth Hoffman[2], Yinhuai Chen[4], Vikram Prasad[4], Stephen C. Linn[1], Rafael J. Tamargo[9], Wendy Westbroek[9], Ellen Sidransky[9], Dimitri Krainc[7,8] and Gary E. Shull[4]

[1]Department of Biological Sciences and [2]Department of Psychological Science, Northern Kentucky University, Highland Heights, KY 41099, USA, [3]Department of Psychology and Neurology and [4]Department of Molecular Genetics, Biochemistry, and Microbiology, University of Cincinnati, Cincinnati, OH 45267, USA, [5]Department of Neuroscience and Center for Translational Research in Neurodegenerative Disease, University of Florida, Gainesville, FL 32610, USA, [6]Department of Neuroscience, Mayo Clinic, Jacksonville, FL 32224, USA, [7]Department of Neurology, Massachusetts General Hospital, Harvard Medical School, Boston, MA 02114, USA, [8]Mass General Institute for Neurodegenerative Disease, Charlestown, MA 02129, USA, and [9]Section on Molecular Neurogenetics, Medical Genetics Branch, National Human Genome Research Institute, National Institutes of Health, Bethesda, MD 20892, USA

Received December 12, 2012; Revised January 29, 2013; Accepted February 4, 2013

Mutations in *ATP13A2* (PARK9), encoding a lysosomal P-type ATPase, are associated with both Kufor–Rakeb syndrome (KRS) and neuronal ceroid lipofuscinosis (NCL). KRS has recently been classified as a rare genetic form of Parkinson's disease (PD), whereas NCL is a lysosomal storage disorder. Although the transport activity of ATP13A2 has not been defined, *in vitro* studies show that its loss compromises lysosomal function, which in turn is thought to cause neuronal degeneration. To understand the role of ATP13A2 dysfunction in disease, we disrupted its gene in mice. *Atp13a2*$^{-/-}$ and *Atp13a2*$^{+/+}$ mice were tested behaviorally to assess sensorimotor and cognitive function at multiple ages. In the brain, lipofuscin accumulation, α-synuclein aggregation and dopaminergic pathology were measured. Behaviorally, *Atp13a2*$^{-/-}$ mice displayed late-onset sensorimotor deficits. Accelerated deposition of autofluorescent storage material (lipofuscin) was observed in the cerebellum and in neurons of the hippocampus and the cortex of *Atp13a2*$^{-/-}$ mice. Immunoblot analysis showed increased insoluble α-synuclein in the hippocampus, but not in the cortex or cerebellum. There was no change in the number of dopaminergic neurons in the substantia nigra or in striatal dopamine levels in aged *Atp13a2*$^{-/-}$ mice. These results show that the loss of Atp13a2 causes sensorimotor impairments, α-synuclein accumulation as occurs in PD and related synucleinopathies, and accumulation of lipofuscin deposits characteristic of NCL, thus providing the first direct demonstration that null mutations in *Atp13a2* can cause pathological features of both diseases in the same organism.

INTRODUCTION

ATP13A2 (*PARK9*) encodes a lysosomal P_5-ATPase of undetermined substrate specificity (1,2). Mutations in *ATP13A2* are associated with Kufor–Rakeb syndrome (KRS), a juvenile onset, autosomal recessive Parkinsonism in humans (3), and are also associated with both adult onset neuronal ceroid

*To whom correspondence should be addressed. Tel: +1 8595725933; Fax: +1 8595725639; Email: schultheisp@nku.edu

lipofuscinosis (NCL) in dogs (4,5) and juvenile onset NCL in humans (6). KRS patients display motor deficits, including rigidity and bradykinesia, and by brain imaging show pallidopyramidal degeneration followed later by widespread cerebral atrophy (7–9). NCLs are a group of neurodegenerative diseases characterized by the accumulation of autofluorescent storage material (ceroid lipofuscin) within lysosomes of neurons and other cell types. Common clinical features include motor deterioration (cerebellar ataxia), dementia, seizures and visual impairment (4,5,10). Of particular interest is a recent study showing that a juvenile onset form of NCL was caused by an *ATP13A2* missense mutation (6). Affected individuals developed typical NCL pathology (11) but also presented with clinical features commonly seen in KRS (12), suggesting that KRS and NCL are related disorders in which lysosomal dysfunction plays a central role (6).

Insights into the function of ATP13A2 have come from studies in yeast, *Caenorhabditis elegans* and mammalian cell lines. Ypk9p, the yeast homologue of human ATP13A2, protects yeast cells from Mn^{2+} toxicity (13,14). Similarly, ATP13A2 protects mammalian cell lines and rat primary neuronal cultures from Mn^{2+}-induced cell death, thus establishing a link between ATP13A2 activity and an environmental risk factor (manganese exposure) for Parkinsonism (15). Studies also demonstrate a potential protective function of ATP13A2 against α-synuclein toxicity in *C. elegans* and rodent primary neuronal cell cultures (14,16). Aggregation of α-synuclein is associated with both inherited and sporadic forms of Parkinson's disease (PD) (17,18), and intratstriatal inoculation of synthetic misfolded fibrilar α-synuclein leads to nigrostriatal cell death *in vivo* (19), suggesting a direct role for α-synuclein in the pathophysiology of PD. Studies in fibroblasts from KRS patients and dopaminergic cell lines show that the loss of ATP13A2 leads to the accumulation of α-synuclein and neurotoxicity *in vitro*, impaired lysosomal acidification and degradation capacity, decreased proteolytic processing of lysosomal enzymes, accumulation and enlargement of lysosomes and decreased clearance of autophagosomes (16,20).

Other investigators (6) have noted that although NCL histopathology has been identified in patients with *ATP13A2* mutations, there are currently no histopathological studies from KRS patients. Thus, it is unclear whether KRS patients develop Lewy body and nigrostriatal pathology similar to that found in PD. To assess the function of *ATP13A2* and its potential role in KRS and NCL, we generated mice with a targeted disruption of the *Atp13a2* gene. These mice were evaluated with a battery of sensorimotor and cognitive tests, and various histological and biochemical analyses were performed to determine whether the loss of Atp13a2 function affected behavior, α-synuclein aggregation, lipofuscin accumulation and nigrostriatal dopaminergic integrity. We show that the loss of Atp13a2 in mice results in sensorimotor deficits in old age, widespread neuronal accumulation of lipofuscin and aggregation of α-synuclein in hippocampus.

RESULTS

Atp13a2 gene targeting

The gene targeting strategy led to a global knockout of *Atp13a2* (Fig. 1A). The deleted exons included sequences encoding the catalytic phosphorylation site (Asp 559), which is essential for enzyme activity. After germline transmission of the targeted allele, heterozygous mice were bred to obtain offspring of all three genotypes. Southern blot (Fig. 1B) and PCR (Fig. 1C) analyses of tail DNA from offspring of a heterozygous mating showed that the *Atp13a2* gene was correctly targeted.

Northern blot analysis (Fig. 2A) revealed a transcript of the expected size in brains of wild-type mice, a truncated transcript in null mutants and wild-type and truncated transcripts at similar expression levels in heterozygous mice. The 2.9 kb mutant transcript hybridized with the Neo and 5′ probes but not with the 3′ probe, indicating that it terminates at an SV40 poly A signal sequence (Fig. 2B), which was included immediately beyond the promoter of the Neo gene to ensure the termination of the transcript. RT–PCR and sequence analysis (Fig. 2C) showed that the donor splice site of exon 11 was spliced to a cryptic acceptor site within the Neo gene, thereby eliminating the last 828 codons of the 1169 codon mRNA, but adding an alternative 168 codons before a stop codon was encountered.

The protein encoded by the mutant mRNA is predicted to consist of the first 341 amino acids of Atp13a2 and 168 amino acids derived from the antisense strand of the Neo gene. Immunoblot analysis using an antibody that would identify both wild-type and mutant proteins detected a 160 kDa band in $Atp13a2^{+/+}$ brain extracts, which was absent in extracts from $Atp13a2^{-/-}$ brains (Fig. 2D). The protein detected in wild-type extracts has an apparent molecular weight that is larger than predicted (127 kDa) on the basis of amino acid sequence, possibly due to post-translational modifications. A non-specific band of 110 kDa was identified in both genotypes; however, a 50–60 kDa protein was not observed in extracts of mutant brains, suggesting that the predicted mutant protein was not stable.

Expression of other P_5-ATPases is unaffected by Atp13a2 ablation

Because all the five P_5-ATPases (*Atp13a1-Atp13a5*) are expressed in the mouse brain, it was important to determine whether compensatory upregulation of *Atp13a1*, *Atp13a3*, *Atp13a4* or *Atp13a5* might occur in the brains of $Atp13a2^{-/-}$ mice. However, northern blot analysis of brain RNA revealed no differences in the expression of any of these genes (Fig. 3), suggesting that compensation by another isoform does not occur.

Gross phenotype

Offspring from heterozygous matings were born at the expected 1:2:1 Mendelian ratios (73 wild-type, 136 heterozygous, 70 homozygous), indicating that the null mutation does not cause embryonic or fetal lethality. Both male and female homozygous mutant mice were fertile. $Atp13a2^{-/-}$ mice grew normally and were indistinguishable from $Atp13a2^{+/+}$ mice in outward appearance, size and behavior until old age. Behavioral problems first became apparent at ∼2 years-of-age, when several mutant animals exhibited an unsteady gait. Consequently, we subjected mice of varying ages to a battery of sensorimotor and cognitive tests including challenging beam,

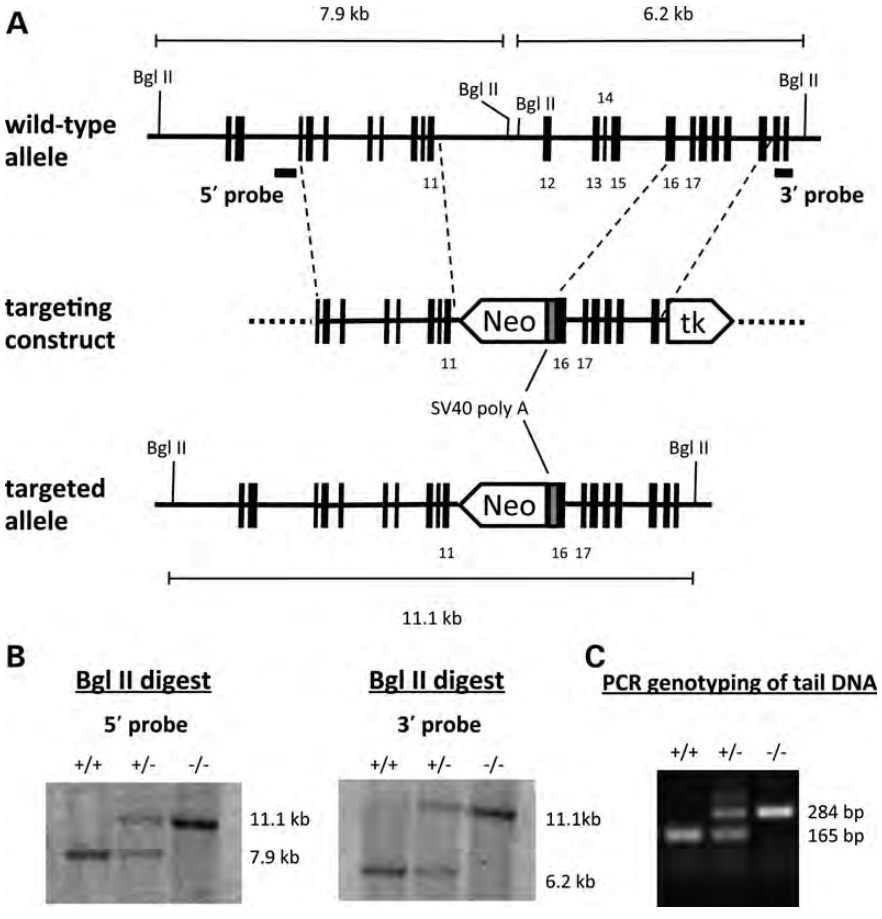

Figure 1. *Atp13a2* gene targeting and genotype analysis. (**A**) Targeting strategy. *Top*, region of the wild-type gene encompassing exons 2–23. *Middle*, targeting construct. Exons 12–15 and a portion of exon 16 were replaced by the Neomycin resistance gene (Neo). The herpes simplex virus thymidine kinase gene (tk) was included for negative selection. Dashed lines represent vector sequences. *Bottom*, predicted structure of the targeted allele. 5′ and 3′ diagnostic probes (solid bars below the wild-type allele) used in the Southern blot analysis and Bgl II restriction fragments unique to the wild-type (7.9 and 6.2 kb) and targeted (11.1 kb) alleles are indicated. (**B**) Southern blot analysis of tail DNA from representative offspring of a heterozygous mating. DNA was digested with Bgl II and hybridized with the 5′ and 3′ outside probes. (**C**) PCR genotyping of tail biopsy DNAs from mice of all three genotypes.

spontaneous activity, gait analysis, nest building, Morris water maze and novel object recognition to determine whether they display behavioral phenotypes characteristic of KRS or NCL.

Challenging beam traversal

At 5–12 months of age, there were no significant differences in time to traverse, number of steps taken while traversing, or the number of errors made on the beam between $Atp13a2^{+/+}$ and $Atp13a2^{-/-}$ mice (Supplementary Material, Fig. S1). However, at 20–29 months of age several differences were noted. Analysis of the mean of five trials showed that $Atp13a2^{-/-}$ mice took more steps and made more errors per step while traversing the beam compared with age-matched $Atp13a2^{+/+}$ mice ($P < 0.05$; Fig. 4A–C). Further analysis in the older cohort by trial was also performed on traversal time, steps and errors per step and showed differences in all three parameters (Fig. 4D–F).

Spontaneous activity

At 5–12 months of age, there were no significant differences in forelimb steps, hindlimb steps, rearing or grooming between $Atp13a2^{+/+}$ and $Atp13a2^{-/-}$ mice (Supplementary Material, Fig. S2). At 20–29 months of age, there were no differences between genotypes in forelimb stepping, rearing or grooming. However, hindlimb stepping was significantly decreased in $Atp13a2^{-/-}$ mice compared with $Atp13a2^{+/+}$ mice ($P < 0.05$; Fig. 5A–D).

Gait analysis

Stride length and stride difference (the variability in stride lengths) were measured in both $Atp13a2^{+/+}$ and $Atp13a2^{-/-}$ mice. Analysis at 5–12 months of age showed no difference in stride length or stride variability between genotypes (Supplementary Material, Fig. S2). Student's *t*-test at 20–29 months comparing genotypes showed that $Atp13a2^{-/-}$ mice made significantly shorter stride lengths compared with wild-type controls. Stride variability scores with females and males combined did not differ between genotypes at 20–29 months, however, analysis of only males ($Atp13a2^{+/+} = 3$, $Atp13a2^{-/-} = 5$) showed that $Atp13a2^{-/-}$ males had significantly more variable stride lengths, which is indicative of ataxic movements (Fig. 5E–F).

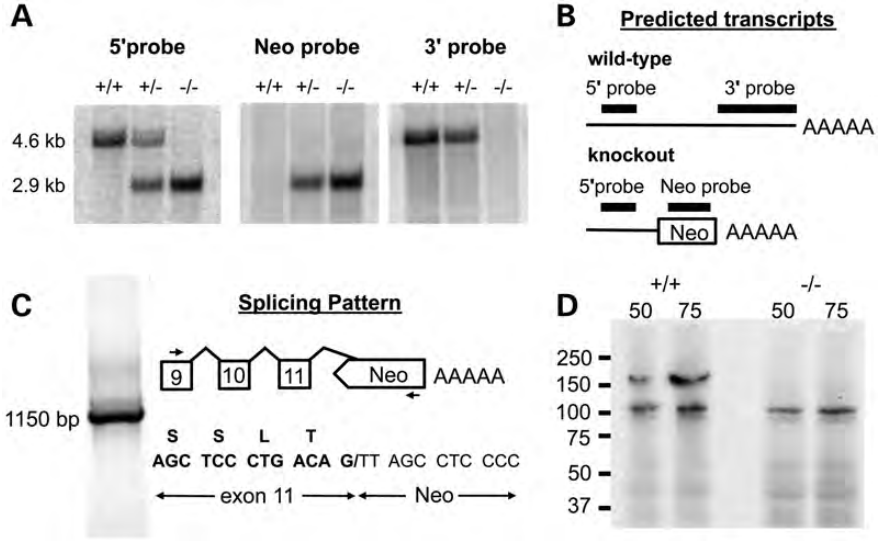

Figure 2. Northern blot and immunoblot analysis of *Atp13a2* transcripts and protein. (**A**) Northern blot analysis of *Atp13a2* transcripts in brain poly(A) RNA of all three genotypes using probes indicated in the schematic diagram (**B**) of wild-type and mutant transcripts. The 2.9 kb mutant transcript hybridizes with the Neo and 5′ probes but not the 3′ probe indicating that it terminates at an SV40 poly(A) signal sequence that precedes sequences from exon 16. (**C**) RT–PCR amplification of mutant first-strand cDNA using primers (small arrows) specific for *Atp13a2* exon 9 and the Neo gene yielded an 1150 bp product. Sequence analysis showed that the donor splice site of exon 11 was spliced to a cryptic acceptor site in the non-coding strand of the Neo gene (top). The region containing the cryptic splice is shown (bottom), with the *Atp13a2* nucleotide sequence and its deduced amino acid sequence in bold. (**D**) Western blot analysis of Atp13a2 protein using brain extracts (50 and 75 μg) from $Atp13a2^{+/+}$ and $Atp13a2^{-/-}$ mice. An antibody directed against amino acids 195–213 of human ATP13A2 detected the wild-type protein (~160 kDa) in $Atp13a2^{+/+}$ but not $Atp13a2^{-/-}$ mice extracts and a non-specific band at 100 kDa in both genotypes, but did not detect a truncated mutant protein in $Atp13a2^{-/-}$ brains.

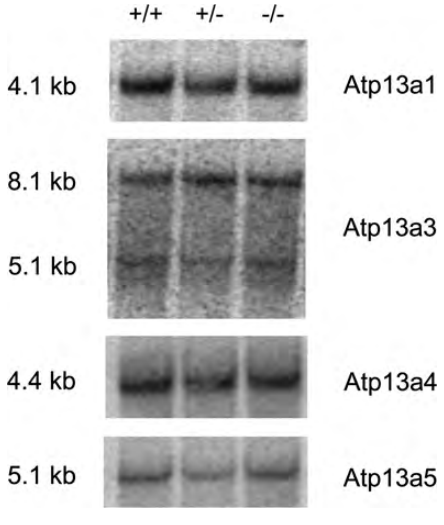

Figure 3. mRNA expression of *Atp13a1*, *Atp13a3*, *Atp13a4* and *Atp13a5* in the brain of wild-type (+/+), heterozygous (+/−) and homozygous (−/−) mutant mice. Northern blot analysis was performed using cDNA probes corresponding to mRNAs for each of the four other *Atp13a* isoforms. Each lane contains 5 μg of poly(A) brain RNA from the mice of the indicated *Atp13a2* genotype. The size of each mRNA, in kilobases, is indicated on the left and the isoform is indicated on the right.

Nest building

The amount of cotton used to build nests was measured in $Atp13a2^{+/+}$ and $Atp13a2^{-/-}$ mice at 20–29 months of age. Mann–Whitney *U* analysis showed that $Atp13a2^{-/-}$ mice used significantly less cotton compared with WT mice ($P < 0.05$; Fig. 6).

Cognitive testing

In addition to sensorimotor deficits, cognitive and neuropsychiatric impairments have been shown to develop in KRS, NCL and PD. Therefore, cognitive function and emotional reactivity were compared between 13–17-month-old $Atp13a2^{-/-}$ and $Atp13a2^{+/+}$ mice in several tests.

In the novel object and spatial recognition task, measures of the time spent exploring a novel object or an object in a novel spatial location minus the time spent investigating the older, matching object did not reveal an effect of genotype (Supplementary Material, Fig. S3A). However, when the total amount of time spent exploring both objects during the familiarization and recognition phase of the test was compared, $Atp13a2^{-/-}$ mice spent significantly more time investigating the objects than the $Atp13a2^{+/+}$ mice ($P < 0.05$; Supplementary Material, Fig. S3B). To further analyze this phenotype, mice were tested in a latency to explore task that assesses how quickly a mouse will move toward the perimeter of a tabletop when placed in the center. While there was no difference between the genotypes in their initiation of movement (Supplementary Material, Fig. S3C) or the percentage of time spent moving while inside of a square (Supplementary Material, Fig. S3D), $Atp13a2^{-/-}$ mice took significantly less time to walk outside of the square in comparison with the $Atp13a2^{+/+}$ mice ($P < 0.05$; Supplementary Material, Fig. S3E). Locomotor activity in an open-field was also measured in $Atp13a2^{-/-}$ and $Atp13a2^{+/+}$ mice. There were no group differences in overall activity or time spent in the center of the cage. Finally, in a light–dark test of anxiety conducted over 3 days, $Atp13a2^{-/-}$ and $Atp13a2^{+/+}$ mice displayed similar patterns of behavior.

In hidden and visible versions of a water-maze task, a two-way analysis of variance comparing the effects of

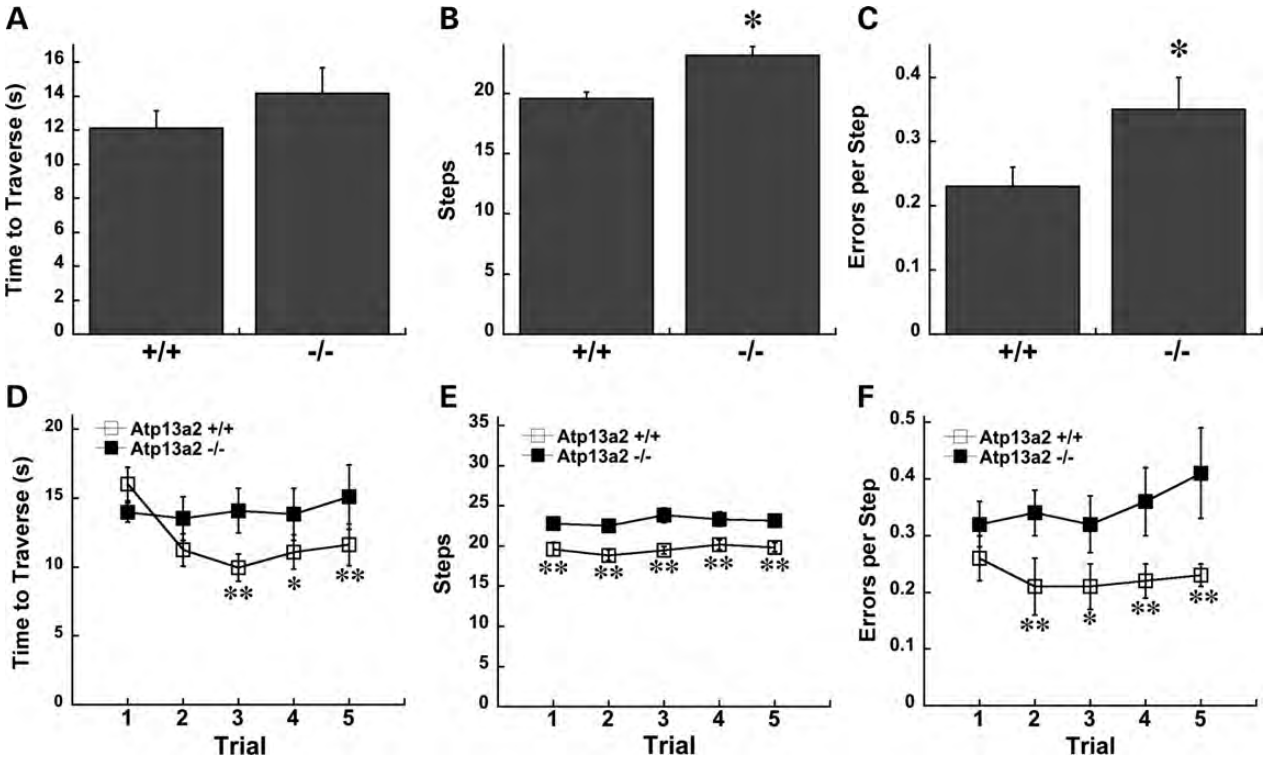

Figure 4. Motor performance and coordination in *Atp13a2*$^{+/+}$ and *Atp13a2*$^{-/-}$ mice at 20–29 months of age. Motor performance and coordination were assessed in *Atp13a2*$^{+/+}$ ($n = 13$) and *Atp13a2*$^{-/-}$ ($n = 18$) mice using a challenging beam test and measured mean time to traverse, number of steps and errors per step (**A**–**C**). Student's *t*-test showed a significant increase in number of steps and errors per step in *Atp13a2*$^{-/-}$ compared with *Atp13a2*$^{+/+}$ mice ($P < 0.05$). Analysis of performance by trial was also measured (**D**–**F**). A 2×5 mixed design ANOVA for traversal time showed a main effect of trial $F_{(4,116)} = 3.83$, $P < 0.01$ and a significant genotype × trial interaction $F_{(4,116)} = 3.98$, $P < 0.01$. *Post hoc* analysis showed that time to traverse between *Atp13a2*$^{+/+}$ and *Atp13a2*$^{-/-}$ mice was comparable during the first two trials; however, *Atp13a2*$^{+/+}$ mice were significantly faster than *Atp13a2*$^{-/-}$ mice during trials 3–5 (T3–T5, $P < 0.05$–0.01). Trial analysis of steps revealed main effects of both genotype $F_{(1,29)} = 12.65$, $P < 0.01$ and trial $F_{(4,116)} = 2.75$, $P < 0.05$ and *post hoc* analysis showed that *Atp13a2*$^{-/-}$ mice made significantly more steps compared with *Atp13a2*$^{+/+}$ mice at each trial (T1–T5 $P < 0.01$). For errors per step, there was a main effect of the genotype $F_{(1,29)} = 4.61$, $P < 0.05$ with *post hoc* analysis showing that *Atp13a2*$^{+/+}$ and *Atp13a2*$^{-/-}$ mice made a similar number of errors per step on the first trial but that *Atp13a2*$^{+/+}$ mice made significantly fewer errors per step compared with mutants in subsequent trials (for T2–T5 $P < 0.05$–0.01). *, **$P < 0.05$, 0.01 compared with *Atp13a2*$^{+/+}$ mice, Fisher's LSD *post hoc*. The values shown are means ± SEM.

genotype and test day did not reveal a significant genotype effect on path length (Supplementary Material, Fig. S4A). A comparison of escape latency over test days revealed a significant effect of the genotype ($P < 0.05$; Supplementary Material, Fig. S4B). *Atp13a2*$^{-/-}$ mice found the platform faster on Days 2 and 3 of testing when compared with the *Atp13a2*$^{+/+}$ mice. There was a trend toward a genotype effect on swim speed ($P = 0.14$, Supplementary Material, Fig. S4C). The mean swim speed in the *Atp13a2*$^{-/-}$ mice was greater on Days 2 and 3 of testing in comparison with the swim speed recorded in the *Atp13a2*$^{+/+}$ mice. No genotype difference was observed in any of the measures taken during the probe trial or visible platform testing.

Stereology and analysis of striatal dopamine content

To determine the effect of the loss of Atp13a2 function on the nigrostriatal dopamine (DA) system, immunohistochemical staining and stereological counting of tyrosine hydroxylase-positive (TH+) neurons in the substantia nigra pars compacta (SNc) was carried out in aged animals (20–29 months). Staining of TH was similar in both genotypes (Fig. 7A and B) and they had a comparable number of TH+ neurons (Fig. 7C; *Atp13a2*$^{+/+}$: 11 760 ± 905; *Atp13a2*$^{-/-}$: 12 704 ± 1054) indicating that the loss of Atp13a2 does not lead to a significant loss of TH-immunoreactive neurons. The total volume of the SNc in *Atp13a2*$^{+/+}$ and *Atp13a2*$^{-/-}$ brains was also similar (Fig. 7D; *Atp13a2*$^{+/+}$: 0.337 ± 0.025 mm^3; *Atp13a2*$^{-/-}$: 0.319 ± 0.022 mm^3). Because changes in DA neurotransmission can occur without loss of dopaminergic neurons *per se*, we also examined striatal DA levels by HPLC. No differences in striatal DA levels or other biogenic amines were observed (Table 1).

Accelerated accumulation of intraneuronal storage material in *Atp13a2*$^{-/-}$ mice

The intraneuronal storage material (lipofuscin) that accumulates in all types of NCL is autofluorescent and stains positively with luxol fast blue (LFB) (21). Compared with *Atp13a2*$^{+/+}$ mice, *Atp13a2*$^{-/-}$ mice show an accelerated deposition of autofluorescent storage material in the cerebellum (Fig. 8A and B) and in the hippocampus at 18 months of age (Fig. 8C and D). Though not as pronounced as in the cerebellum or hippocampus, enhanced autofluorescence was also observed in the cortex (data not shown). The autofluorescent

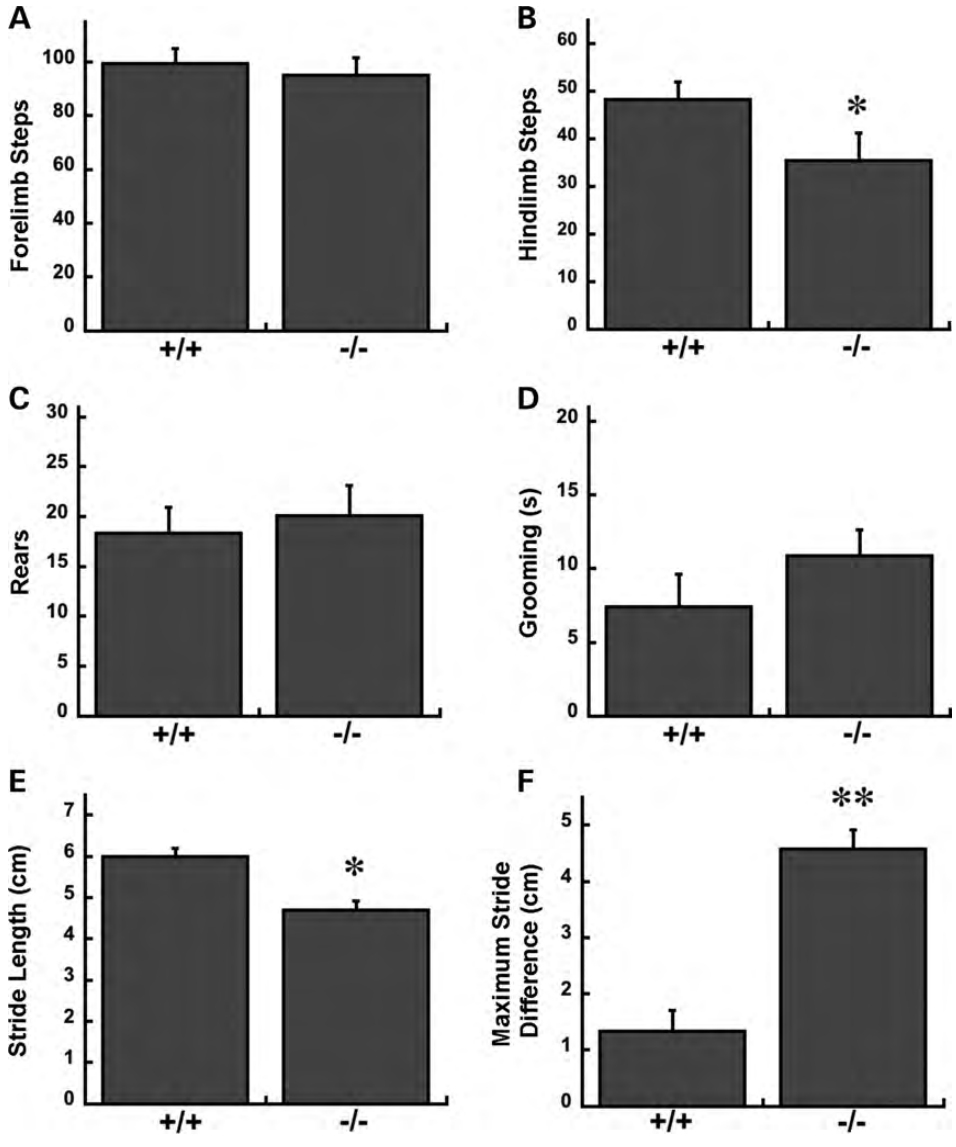

Figure 5. Spontaneous activity and Gait in $Atp13a2^{+/+}$ and $Atp13a2^{-/-}$ mice at 20–29 months of age. Spontaneous activity was assessed in the cylinder and measured forelimb and hindlimb stepping, rears and time spent grooming in $Atp13a2^{+/+}$ ($n = 12$) and $Atp13a2^{-/-}$ ($n = 18$) mice (**A–D**). $Atp13a2^{-/-}$ mice showed a significant reduction in hindlimb stepping compared with $Atp13a2^{+/+}$ mice (B). Gait analyses assessed stride length and stride variability in $Atp13a2^{+/+}$ ($n = 15$) and $Atp13a2^{-/-}$ ($n = 20$) mice (**E** and **F**). $Atp13a2^{-/-}$ mice had a significantly shorter stride length than $Atp13a2^{+/+}$ mice (E). No difference in stride variability was observed when females and males were analyzed together, but when analyzed separately, stride length was significantly more variable in $Atp13a2^{-/-}$ ($n = 5$) than $Atp13a2^{+/+}$ ($n = 3$) males (F). *, **$P < 0.05$, 0.01 compared with Atp13a2$^{+/+}$mice. Student's *t*-test. The values shown are means ± SEM.

signal was quenched with Sudan black staining (data not shown) and the storage material was also visualized by Luxol fast blue-periodic acid Schiff-hematoxylin (LFB-PAS) staining (Fig. 8E–H), both of which are characteristic of lipofuscin.

Accumulation of insoluble α-synuclein in hippocampus of *Atp13a2*$^{-/-}$ mice

Accumulation of aggregated, insoluble α-synuclein within the central nervous system is a characteristic feature of PD. To determine whether the loss of Atp13a2 leads to changes in the levels of soluble and insoluble α-synuclein species, homogenates prepared from the hippocampus (Fig. 9A–C), cortex (Fig. 9D–F) and cerebellum (Fig. 9G–I) were subjected to sequential extraction, first in Triton X-100 buffer and then in 2% SDS buffer, and analyzed by western blot analysis. Increased levels of Triton X-100 insoluble α-synuclein were observed in the hippocampus of $Atp13a2^{-/-}$ mice (Fig. 9A and B). However, no change in α-synuclein protein solubility was observed in either the cortex (Fig. 9D and E) or cerebellum (Fig. 9G and H). The levels and solubility of tau and huntingtin, proteins prone to aggregation in other neurodegenerative disorders, were not significantly changed in any of the brain regions analyzed. These results suggest that the loss of Atp13a2 results in the preferential accumulation of α-synuclein in the hippocampus.

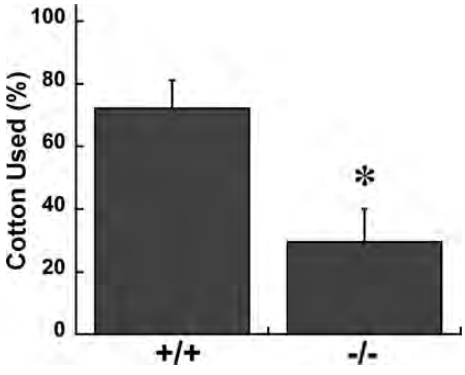

Figure 6. Nestbuilding in *Atp13a2*$^{+/+}$ and *Atp13a2*$^{-/-}$ mice at 20–29 months of age. Complex orofacial and fine motor skills were assessed in *Atp13a2* $^{+/+}$ ($n = 12$) and *Atp13a2*$^{-/-}$ ($n = 17$) mice using a nestbuilding test. The amount of nestbuilding material was measured over a 24 h period. Mann–Whitney *U* analysis showed that *Atp13a2*$^{-/-}$ mice used significantly less cotton compared with *Atp13a2*$^{+/+}$ mice ($P < 0.05$). The values shown are means ± SEM.

Glucocerebrosidase enzyme activity is not significantly down-regulated in Atp13a2$^{-/-}$ mouse brains

It has been suggested that glucocerebrosidase (GCase) enzyme activity and protein levels are reduced in brain samples from patients with PD and Parkinson mouse models (22–25). We measured GCase activity in brain lysates from five Atp13a2$^{+/+}$ and four Atp13a2$^{-/-}$ mice at 20–23 months of age and three Atp13a2$^{+/+}$ and three Atp13a2$^{-/-}$ mice at 16–18 months of age. Within the different age groups, there was no significant difference in GCase enzyme activity detected between genotypes (Supplementary Material, Fig. S5A). The activity of acid alpha-glucosidase (GAA), the enzyme involved in the breakdown of lysosomal glycogen (26), was measured as a control for lysosomal activity and no significant differences were observed (Supplementary Material, Fig. S5B). Furthermore, when measuring the GCase protein content in the different mouse brains with a previously described GCase-specific fluorescent probe (27), no significant difference between genotypes was detected among animals of the same age (Supplementary Material, Fig. S6).

Quantitative RT–PCR array analyses

To determine whether the loss of Atp13a2 leads to changes in the expression of genes implicated in PD and autophagy, gene expression levels in the striatum and SN of *Atp13a2*$^{+/+}$ and *Atp13a2*$^{-/-}$ mice were compared using autophagy and Parkinson's RT^2 Profiler PCR arrays (SABiosciences). The expression of *Nr4a2 (Nurr1)* and brain-derived neurotrophic factor (*Bdnf*) was down-regulated 6.14 and 3.16-fold, respectively, in the striatum of *Atp13a2*$^{-/-}$ mice but unchanged in the SN. *Slc6a3* (dopamine transporter, *DAT*) and tyrosine hydroxylase (Th) expression did not change in either brain region, whereas *Snca* (α-synuclein) was significantly down-regulated in the striatum, but only by 1.15-fold (Table 2). The expression of cathespsin S (Ctss), tumor necrosis factor α (Tnf) and Irgm1 (immunity-related GTPase family, M1) was up-regulated 1.75, 1.60 and 1.56-fold, respectively, in the SN of *Atp13a2*$^{-/-}$ mice (Table 3). Similar expression results were obtained for these genes in the striatum but the results were based on only two animals of each genotype and are not reported in the table.

DISCUSSION

The *Atp13a2*-null mouse model was developed using a global targeting strategy that eliminated much of the coding sequence from the mutant mRNA, including exons encoding the catalytic phosphorylation site, the ATP binding site and most of the transmembrane domains. The mutant and wild-type mRNAs were expressed at similar levels in heterozygous mice, indicating that non-sense-mediated decay does not contribute to degradation of the mutant mRNA, as reported for an *ATP13A2* mutation in humans (28). For some *ATP13A2* mutations, there is evidence that the expression or accumulation of the mutant protein and resulting neurodegeneration from endoplasmic reticulum stress might contribute to the disease phenotype (3,29). Despite the stability of the mRNA, however, a mutant protein was not detected, suggesting that the protein is rapidly degraded or that the mutant mRNA is inefficiently translated. Thus, the phenotype of the mouse model is likely due to lysosomal dysfunction resulting from the loss of Atp13a2, with little, if any, contribution from secondary effects of a mutant protein.

Homozygous or compound heterozygous mutations in *ATP13A2* are now known to cause both Kufor–Rakeb syndrome (3) and NCL (6). The clinical presentation in KRS varies among patients but can include bradykinesia, rigidity, ataxia, dementia, spasticity and supranuclear gaze palsy (8,30–32). To date only one family with NCL has been linked to mutations in *ATP13A2* (6). In an earlier study, members of this Belgian family variably presented with rigidity, akinesia, resting tremor, uncoordinated movements and impaired intellect (11), a spectrum of symptoms that overlap with those of individuals affected by KRS. The Tibetan terrier model of NCL has also been associated with mutations in *ATP13A2*, and develops behavioral problems such as mild ataxia, confusion and occasional aggressiveness (33,34); however, Parkinsonian features, such as bradykinesia, rigidity and tremor, have not been reported in affected dogs (4,5). Therefore, wild-type and mutant mice were subjected to a variety of sensorimotor and cognitive tests at different ages.

Sensorimotor function was measured using tests sensitive to varying types of motor dysfunction and included challenging beam traversal, spontaneous activity, gait and nest building (35–37). Sensorimotor function did not differ between genotypes at 5–12 months of age; however, at 20–29 months of age *Atp13a2*$^{-/-}$ mice displayed significant impairments in all of the motor tests. On the beam mutant mice made more errors per step compared with wild-type mice and analysis of trial-by-trial performance revealed potential motor learning deficits as well. In the trial-by-trial analysis, both genotypes made a similar number of errors on the first trial, but while wild-type mice improved performance on subsequent trials, *Atp13a2*$^{-/-}$ mice did not. A similar pattern was also observed in time to traverse, suggesting the aged mutant mice have impaired aspects of motor learning. In addition, *Atp13a2*$^{-/-}$ mice showed reduced hindlimb stepping in the cylinder, and exhibited impairments in fine motor skills and orofacial

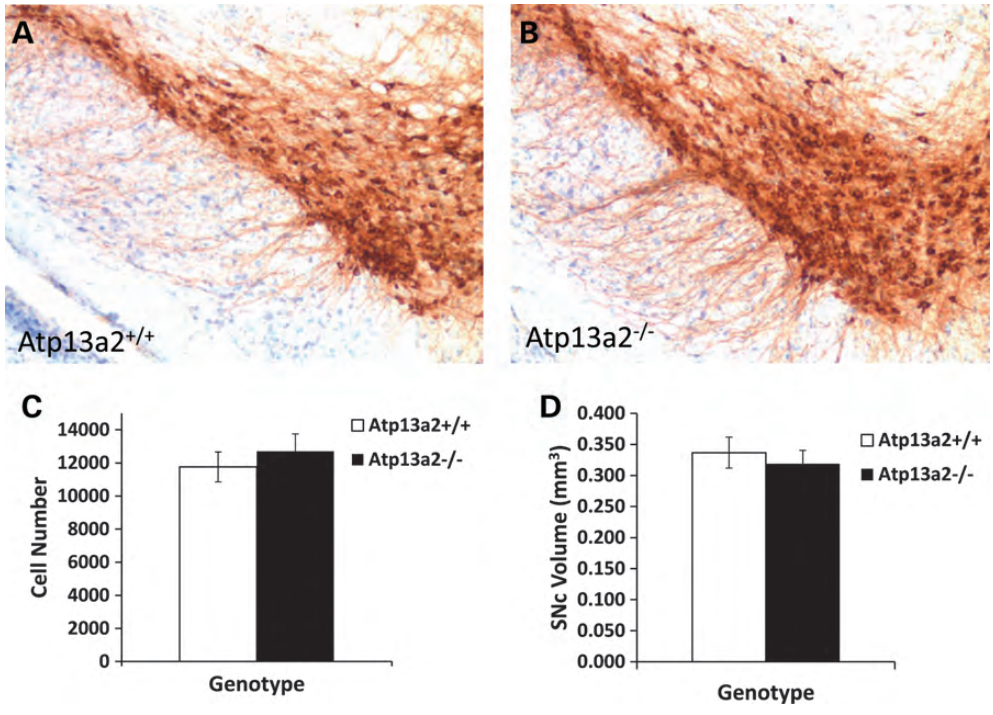

Figure 7. Tyrosine hydroxylase immunostaining and stereological analysis. TH immunostaining of representative mid-brain sections showing dopaminergic neurons in the SNc of *Atp13a2*$^{+/+}$ (**A**) and *Atp13a2*$^{-/-}$ (**B**) mice at 27 months of age; sections were counterstained with cresyl violet; ×100 magnification. (**C**) Average number of tyrosine hydroxylase-positive neurons in the SNc of *Atp13a2*$^{+/+}$ and *Atp13a2*$^{-/-}$ mice at 22–27 months of age and (**D**) volume of SNc in the same mice, as determined by stereological analysis. $n = 6$ mice of each genotype for all analyses. The values shown are means ± SEM.

Table 1. Striatal biogenic amine concentrations

	Norepinephrine	DOPAC	DA	5-HIAA	HVA	5-HT
Atp13a2$^{+/+}$	1.34 ± 0.36	8.50 ± 0.41	112.13 ± 7.40	2.81 ± 0.16	9.35 ± 0.56	6.73 ± 0.57
Atp13a2$^{-/-}$	1.64 ± 0.45	8.17 ± 0.69	112.83 ± 10.55	3.31 ± 0.33	9.72 ± 0.82	7.28 ± 0.98

Values are given in ng/mg protein and represent the average ± SEM. $n = 10$ for each genotype; mice were 20–29 months of age. DOPAC, 3,4-dihydroxyphenylacetic acid; DA, dopamine; 5-HIAA, 5-hydroxyindole acetic acid; HVA, homovanillic acid; 5-HT, 5-hydroxytryptamine (serotonin).

movements involved in nestbuilding. In analyses of gait, aged mutant mice exhibited a shortened stride length and while there was no statistical difference in the variability of stride lengths between genotypes, there was a slight trend for mutants to have more variable stride lengths. However, when males and females were analyzed separately we found male *Atp13a2*$^{-/-}$ mice had significantly more variable stride lengths compared with male *Atp13a2*$^{+/+}$ mice suggesting ataxia-like movements in aged males. The sensorimotor deficits observed in aged mutant mice are similar to deficits seen in genetic mouse models of PD and ataxia (36–38) and resemble aspects of motor dysfunction observed in KRS, NCL and PD.

Cognitive function and emotional reactivity were also compared in *Atp13a2*$^{-/-}$ and *Atp13a2*$^{+/+}$ mice. In the water-maze task, mutant mice found the platform faster, which would typically indicate improved spatial learning capacity and hippocampal function. However, the improved escape latency was likely due to mean increases in swim speed displayed by the mutant mice. Moreover, the distance traveled before finding the platform did not distinguish mutant and wild-type mice. In the object recognition and latency to explore tests, mutant mice demonstrated greater exploratory/investigatory activities that were not accompanied by changes in general locomotor activity or anxiety, as assessed in open-field and light-dark tests, respectively. It is possible that such changes in exploratory behavior are linked to altered hippocampal function. Hippocampal neurons fire during spatial exploration (39,40), and it is possible that lipofuscin and α-synuclein accumulation in or near these neurons disrupts their spatial processing function. It is noteworthy that enhanced exploration has also been observed in other mouse models of PD (41), suggesting that different cellular pathways implicated in PD can lead to a similar behavioral phenotype.

Although there is currently no reported postmortem analysis of brain histopathology in KRS, imaging studies show that some patients develop diffuse cerebral and cerebellar atrophy and decreased DAT activity in the striatum, but there is no evidence of abnormalities in the SN (42,43). In the one known family with *ATP13A2*-associated NCL in

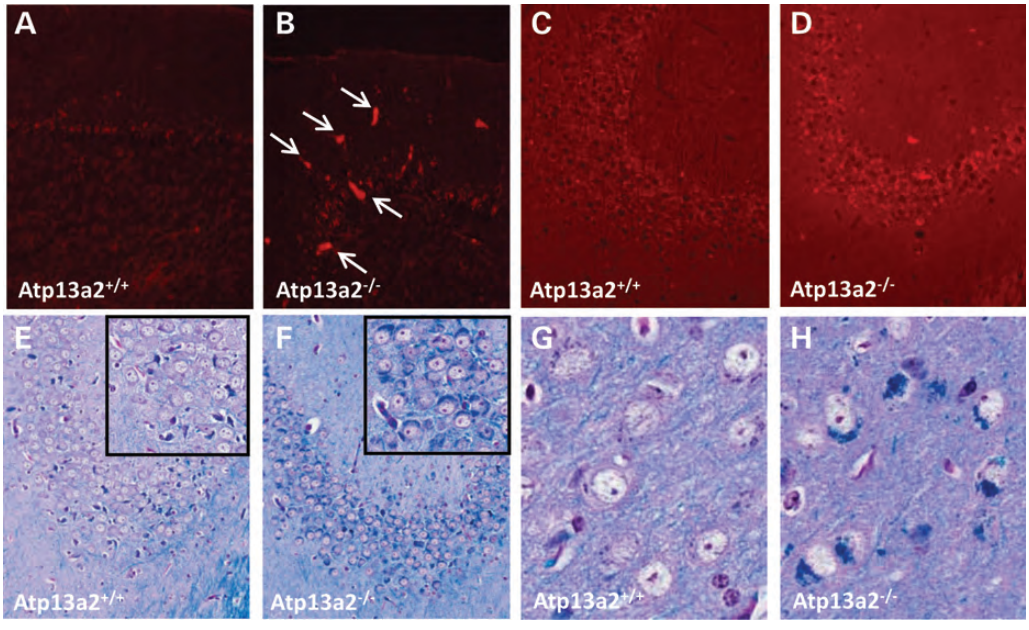

Figure 8. Accelerated accumulation of intraneuronal storage material (lipofuscin) in the cerebellum, hippocampus and cortex of *Atp13a2*$^{-/-}$ mice. Autofluorescent storage material in the cerebellum **(A** and **B)**, and in neurons of the CA-3 region of the hippocampus **(C** and **D)** of an 18-month-old *Atp13a2*$^{-/-}$ mouse and age-matched control; representative fluorescence images of 7 μm paraffin sections are shown. Particularly large autofluorescent inclusions (arrows) were seen in the cerebellum of *Atp13a2*$^{-/-}$ mice (**E**–**H**). LFB-PAS stained paraffin sections. Lipofuscin staining (dark blue) is markedly increased in *Atp13a2*$^{-/-}$ brain neurons relative to controls. Sections from the hippocampus (E and F) and the cortex (G and H) are shown.

humans, brain histopathology has not been reported, but in a peripheral nerve biopsy these patients exhibited autofluorescent inclusions (11). In canine NCL, diffuse atrophy in the brain and accelerated accumulation of autofluorescent storage material, or lipofuscin, has been shown in both the cortex and the cerebellum (4). Lipofuscin develops in the lysosomes of cells over the course of aging and accumulates preferentially in the cytosol of postmitotic cells. Its formation is negatively associated with cell survival (44–46) and it is known from lysosomal storage disorders that substantial deposition of lipofuscin is associated with cellular dysfunction (47). Therefore, we measured autofluorescent material in multiple brain regions of *Atp13a2*$^{-/-}$ mice. We found enhanced autofluorescence and luxol blue-positive staining indicative of lipofuscin in the cortex, cerebellum and the CA3 region of the hippocampus in *Atp13a2*$^{-/-}$ mice compared with age-matched controls. Thus, the results of the current study, and previous studies of ATP13A2-deficiency in dogs and humans, clearly demonstrate that the loss of this P-type ATPase causes lipofuscinosis in all three species.

A characteristic feature of PD is the accumulation of aggregated forms of α-synuclein (48,49). Although there is no confirmation of α-synuclein pathology in KRS or *ATP13A2*-associated NCL, dysfunction of the lysosomal degradation pathway is associated with both PD and α-synuclein aggregation. For example, mutations in GCase cause Gaucher's disease, a rare inherited lysosomal storage disorder, and are the most common genetic risk factor for PD (50,51). The lysosomal degradation pathway is particularly important for clearance of aggregated α-synuclein (52), and studies in yeast (14) and in mammalian cell culture, including mouse primary cortical neurons and rat primary mesencephalic dopaminergic neurons, show that the loss of Atp13a2 function results in α-synuclein aggregation and cellular toxicity (16,20). Consistent with those studies, we show for the first time that depletion of Atp13a2 *in vivo* leads to the accumulation of α-synuclein in the mouse brain. Loss of Atp13a2 did not cause changes in levels of soluble α-synuclein in the hippocampus, cortex or cerebellum, but did result in ∼3-fold increase in Triton-insoluble α-synuclein in the hippocampus. It is important to note that lipofuscin accumulation in *Atp13a2*$^{-/-}$ brains was most pronounced in the hippocampus, where α-synuclein accumulation was also observed. This suggests that there may be a relationship, most likely lysosomal dysfunction, between lipofuscin accumulation and the formation of insoluble α-synuclein. Tau and huntingtin proteins were also analyzed and showed no changes in protein solubility, indicating that the loss of Atp13a2 causes specific aggregation of α-synuclein. These results highlight the functional importance of *Atp13a2* in lysosomal degradation of α-synuclein in a mammalian brain *in vivo*. Recent studies have also shown that GCase enzyme activity is reduced in PD patients (22–27). Therefore, we examined GCase enzyme activity and protein levels in whole brain extracts from *Atp13a2*$^{-/-}$ and *Atp13a*$^{+/+}$ mice. However, no significant differences were observed across genotypes. It will be worthwhile in future studies to measure GCase enzyme activity and protein levels in specific brain regions of the knockout mice.

We also compared the expression of genes implicated in PD and autophagy in the striatum and SN of *Atp13a2*$^{+/+}$ and *Atp13a2*$^{-/-}$ mice at 8–15 months of age using pathway-specific real-time PCR arrays. The observed down-regulation of *Nurr1* and *Bdnf* in the striatum of *Atp13a2*$^{-/-}$ mice is particularly noteworthy as these genes play an important role in the development and maintenance of dopaminergic neurons (53,54). Moreover, previous studies have shown that *Nurr1*

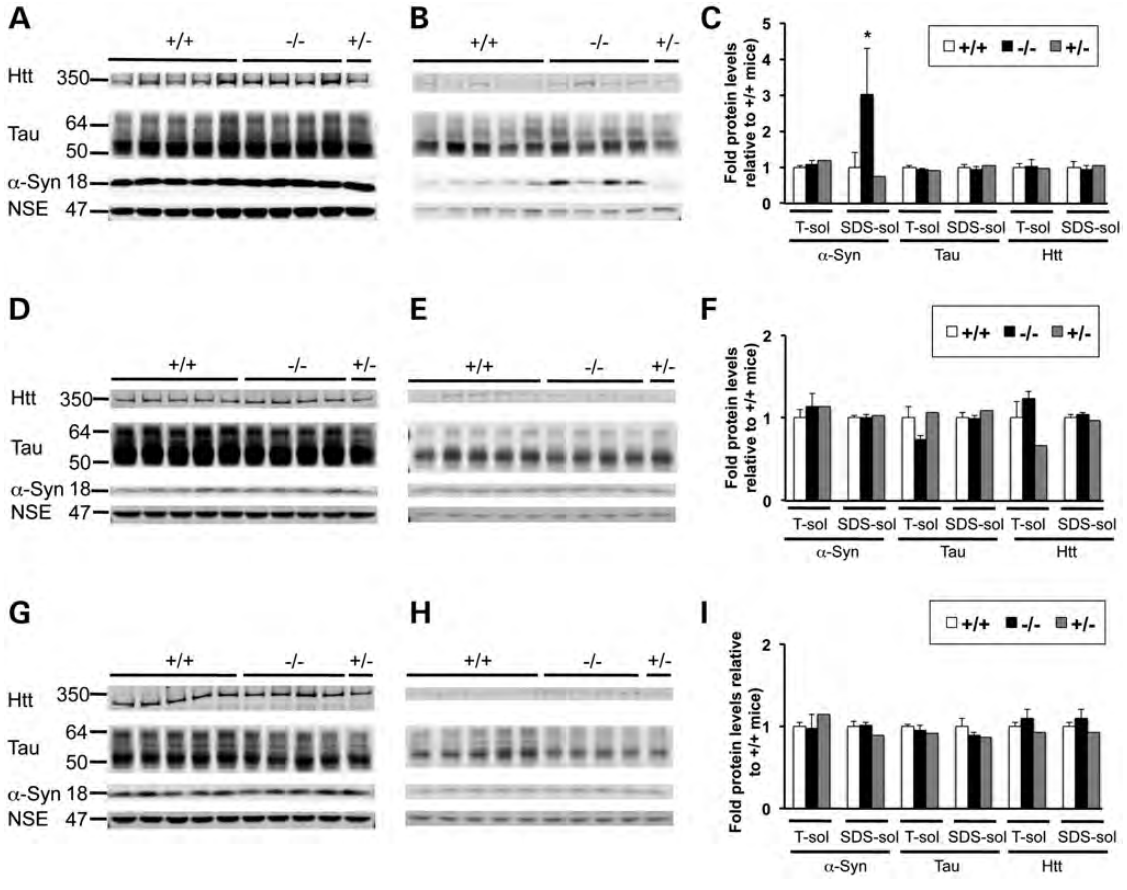

Figure 9. α-Syn accumulation in hippocampus of *Atp13a2*$^{-/-}$ mice. Western blot analysis of T-sol (**A**, **D** and **G**) and SDS-sol fractions (**B**, **E** and **H**) from hippocampal (A and B), cortical (D and E) and cerebellar (G and H) lysates. Endogenous α-synuclein, tau and huntingtin levels were compared in lysates prepared from *Atp13a2*$^{+/+}$ ($n = 5$), *Atp13a2*$^{-/-}$ ($n = 4$) and *Atp13a2*$^{+/-}$ ($n = 1$) mice at 18–20 months of age. Relative protein levels in the hippocampus (**C**), cortex (**F**) and cerebellum (**I**) are shown in the panels to the right of the blots (*$P < 0.03$). Neuron-specific enolase (NSE) was used as a loading control. The values shown are means ± SEM.

expression is decreased in PD and may play an important role in the pathogenesis of the disease (53). Though it is unclear why these genes are down-regulated in the striatum and not the SN, it suggests that the loss of Atp13a2 leads to perturbations in the basal ganglia region of the brain. Indeed, imaging studies suggest iron accumulation in caudate and putamen in KRS (42,43). It is also noteworthy that the absence of changes in *Nurr1* expression in the SN is consistent with the analysis of nigrostriatal integrity showing no differences in nigrostriatal dopaminergic neuron numbers or in the striatal DA content in the mutant mice (53).

Because the behavioral phenotype was not detectable until old age, it seemed possible that it might be modulated to some extent by compensatory mechanisms associated with other members of the P_5-ATPase family. We examined mRNA levels for the other members of the P_5-ATPase family (Atp13a1 and Atp13a3-5) and found no compensatory up-regulation. This was not surprising, as there is no evidence that the other isoforms are expressed in lysosomes and, in fact, the yeast homologue of ATP13A1 is expressed in the endoplasmic reticulum (55). Furthermore, there is suggestive evidence that substrate specificities may differ between isoforms. As noted previously (1), P-type pumps that share the same substrate specificity and stoichiometry, such as isoforms of the sarco(endo)plasmic reticulum Ca^{2+}-ATPase, plasma membrane Ca^{2+}-ATPase or Na^+,K^+-ATPase, have a high degree of amino acid sequence identity in their transmembrane domains. In contrast, for the P_5-ATPases, including those whose genes are tandemly linked on the same chromosome, the transmembrane domains exhibit a high degree of sequence divergence (1). This suggests that ATP13A2 and the other P_5-ATPases, rather than transporting a specific inorganic cation, may transport substrates belonging to a general class of molecules, with each isoform having different substrate specificities. Other investigators have also speculated that ATP13A2 may transport substrates other than inorganic cations, such as a cofactor for lysosomal enzymes (56), or that its transport activity might affect lysosomal pathways for ceramide metabolism (57). This is a reasonable hypothesis, as some P_4-ATPases are known to mediate phospholipid translocation (58) and the yeast homolog of ATP13A1 affects regulation of the HMG-CoA reductase, a critical enzyme of the mevalonate pathway (59), raising the possibility that it handles lipid substrates. Further studies are needed to address this important issue.

In summary, our data show that the loss of Atp13a2 in mice leads to lipofuscinosis that is a critical feature of NCL and supports recent *in vitro* studies showing that ATP13A2 deficiency compromises lysosomal function and results in both

Table 2. Parkinson's PCR array

Gene	ΔC_T ($n = 6$) *Atp13a2*$^{+/+}$	*Atp13a2*$^{-/-}$	Expression relative to +/+	Fold regulation relative to +/+
Striatum				
Nr4a2	6.29 ± 0.36	8.91 ± 0.57	0.163*	−6.14
Bdnf	9.01 ± 0.26	10.68 ± 0.45	0.316*	−3.16
Slc6a3	11.39 ± 0.14	11.71 ± 0.24	0.801	−1.25
Snca	0.79 ± 0.03	0.99 ± 0.02	0.871**	−1.15
Th	8.64 ± 0.14	8.74 ± 0.08	0.936	−1.07
	ΔC_T ($n = 4$) *Atp13a2*$^{+/+}$	*Atp13a2*$^{-/-}$	Expression relative to +/+	Fold regulation relative to +/+
Substantia nigra				
Nr4a2	6.10 ± 0.27	6.06 ± 0.08	1.03	1.03
Bdnf	7.89 ± 0.27	8.04 ± 0.38	0.901	−1.11
Slc6a3	2.45 ± 0.21	2.33 ± 0.20	1.09	1.09
Snca	3.13 ± 0.22	3.38 ± 0.15	0.844	−1.19
Th	4.84 ± 0.29	4.71 ± 0.25	1.10	1.10

The *Nr4a2* and *Bdnf* genes are down-regulated in the striatum but not the substantia nigra of *Atp13a2*$^{-/-}$ mice. Values obtained from Parkinson's RT^2 Profiler PCR array analysis of tissues from wild-type and *Atp13a2*$^{-/-}$ animals. ΔC_T represents the difference in cycle threshold between the mRNA of interest and the average of a set of housekeeping mRNAs whose expression was found not to vary as a function of the *Atp13a2* genotype. Values are shown as mean ± SEM and the number of replicates is indicated. Expression relative to +/+ is the mean normalized gene expression ($2^{-\Delta CT}$) in the −/− replicates divided by the mean normalized expression in the +/+ replicates. Differences in expression that were found to be significant are marked with one ($P < 0.05$) or two ($P < 0.005$) asterisks. Fold regulation is equal to relative expression for values ≥1 and to the negative reciprocal of relative expression for values <1.

Table 3. Autophagy PCR array

Gene	ΔC_T ($n = 4$) *Atp13a2*$^{+/+}$	*Atp13a2*$^{-/-}$	Expression relative to +/+	Fold regulation relative to +/+
Substantia nigra				
Ctss	3.09 ± 0.05	2.28 ± 0.12	1.75**	1.75
Tnf	13.86 ± 0.09	13.18 ± 0.25	1.60*	1.60
Irgm1	6.92 ± 0.12	6.28 ± 0.15	1.56*	1.56

The *Ctss*, *Tnf* and *Irgm1* genes are up-regulated in the substantia nigra of *Atp13a2*$^{-/-}$ mice. Values obtained from Autophagy RT^2 Profiler PCR array analysis of tissue from wild-type and *Atp13a2*$^{-/-}$ animals. ΔC_T represents the difference in cycle threshold between the mRNA of interest and the average of a set of housekeeping mRNAs whose expression was found not to vary as a function of the *Atp13a2* genotype. Values are shown as mean ± SEM and the number of replicates is indicated. Expression relative to +/+ is the mean normalized gene expression ($2^{-\Delta CT}$) in the −/− replicates divided by the mean normalized expression in the +/+ replicates. Differences in expression that were found to be significant are marked with one ($P < 0.05$) or two ($P < 0.005$) asterisks. Fold regulation is equal to relative expression for values ≥1 and to the negative reciprocal of relative expression for values <1.

lipofuscinosis and abnormal accumulation of α-synuclein (14,16,20). Additionally, these mice will serve as a useful model for clarifying the relationship between NCL and KRS and furthering our understanding of the pathogenic mechanisms underlying these disease states, and others, such as PD.

MATERIALS AND METHODS

Generation of mutant mice

A replacement-type vector was used to exchange exons 12–15 and the 5′ half of exon 16 with a neomycin resistance (Neo) gene, which was in the opposite orientation relative to the *Atp13a2* transcription unit. Homologous arms flanking the Neo gene were amplified by PCR from mouse genomic DNA. The 3.2 kb 5′ arm was amplified using forward (5′-GGTGCAGAC TGAGGCTGTTGTTCAG-3′) and reverse (5′-TCCTGCATTAT GCAGAGTCTCAGCC-3′) primers complementary to sequences in exon 4 and intron 11, respectively, whereas the forward (5′-GCTTGGACGTAATGGGCGTGGTGC-3′) and reverse primers (5′-GATGACAAGGAATGGGGTCACTCTG-3′) used to amplify the 2.2 kb 3′ arm correspond to sequences in exon 16 and intron 21. Gene targeting and blastocyst-mediated transgenesis were performed using standard protocols, and chimeras were bred with Black Swiss mice to obtain ES cell-derived offspring. The mice are available to interested researchers directly through the corresponding author.

Southern blot analysis and PCR genotyping

Southern blot analysis of ES cell and mouse tail DNA was carried out as described previously (60). The 419 base pair (bp) 5′ probe began at nucleotide (nt) 879 of intron 3 and ended at nt 22 of exon 4, and the 304 bp 3′ probe began at nt 98 of intron 21 and ended at nt 80 of exon 23. Primers used to amplify the probes were as follows: 5′ probe, (5′-AGGATGCTTGCTGCATAGGTG-3′ and 5′-TGAAGAGCTGTCTGGAGCTAC-3′); 3′ probe, (5′-CT GAGCTGAGTTTCCTGACTG-3′ and 5′-TGAAGCCTCTGCA GTTCGCAC-3′). PCR genotyping was performed using DNA from tail biopsies. Forward (5′-AACACTCCGTGCTTCAGTT TCC-3′) and reverse (5′-AAGGACACGGGACGCAAGCAG-3′) primers corresponding to nucleotides 133–154 and 277–297 of intron 11, respectively, amplified a 165 bp product from the wild-type gene. A reverse primer (5′-CCAATACGCCCGC GTTTCTTCC-3′) complementary to sequences within the Neo gene, and the forward primer described above amplified a 284 bp product from the targeted allele.

RNA isolation and northern blot analysis

Total RNA and Poly(A) RNA was isolated using Tri-Reagent and Oligo (dT)-Cellulose Columns (Molecular Research

Center, Inc.). Poly(A) RNA (5 μg) was denatured with glyoxal and dimethyl sulfoxide, fractionated in 1% agarose and transferred to a nylon membrane. Hybridization with ^{32}P-labeled probes was performed as described previously (60). cDNA probes for wild-type and mutant *Atp13a2* transcripts included 652 bp (5′ probe) and 1775 bp (3′ probe) fragments spanning codons 60–276 and 568–1158, respectively, and a 760 bp probe corresponding to codons 1–240 of the Neo gene. cDNA probes for the other P_5-ATPases (*Atp13a1*, *Atp13a3*, *Atp13a4* and *Atp13a5*) have been described previously (60).

RT–PCR and sequence analysis of the homozygous mutant transcript

Oligo(dT) primed cDNA was generated from *Atp13a2*$^{-/-}$ brain poly(A) RNA (~250 ng) using the Invitrogen SuperScript First-Strand Synthesis System for RT–PCR. PCR amplification was carried out using AccuPrime Taq DNA polymerase (Invitrogen) and primers specific for *Atp13a2* exon 9 (5′-ACTACTGGTATGCTCTCTGC-3′) and the Neo gene (5′-GCATATTAAGGTGACGCGTGTG-3′). The resultant PCR product was purified using a QIAquick Gel Extraction Kit (Qiagen) and sequenced (Retrogen, Inc.).

Western blot analysis

For the detection of Atp13a2 protein, brains were sonicated in 2% SDS, 50 mM Tris–HCl (pH 6.8) and the protein content was determined by the BCA assay. Lysates (50 and 75 μg) were mixed with 4× Laemmli buffer, boiled for 10 min, resolved on a 4–20% acrylamide gel, transferred to nitrocellulose and blocked for 1 h in 5% skim milk in Tris-buffered saline (TBS). The membrane was incubated overnight at 4°C with a 1:500 dilution of rabbit anti-human ATP13A2 antibody (Sigma A9607, which identifies amino acids 195–213), washed and incubated in anti-rabbit horseradish peroxidase labeled secondary antibody (1:5000 dilution) for 1 h at room temperature (RT). After washes in TBS, the membranes were treated with ECL plus reagent for 1 min, and signals were detected with the Protein Simple Imager.

Breeding and behavioral testing

Heterozygous male and female mice were bred together to produce knockout and wild-type mice used in all experiments. Separate cohorts of *Atp13a2*$^{+/+}$ and *Atp13a2*$^{-/-}$ mice were tested at 5–12 and 20–29 months of age for motor performance and coordination, spontaneous activity and gait.

Challenging beam traversal

Motor performance and coordination were measured with the challenging beam traversal test (36,61–65). Briefly, the beam consists of four sections (25 cm each, 1 m total length), each section having a different width. The beam starts at a width of 3.5 cm and gradually narrows by 1 cm increments a final width of 0.5 cm. Animals were trained to traverse the length of the beam starting at the widest section and ending at the narrowest section. Animals received 2 days of training prior to testing; on the day of the test, a mesh grid (1 cm^2) of corresponding width was placed over the beam surface leaving ~1 cm space between the grid and the beam surface. Animals were then videotaped, while traversing the grid-surfaced beam and videotapes were rated in slow motion by an experimenter blind to genotype. Errors, steps and time to traverse the beam were measured across five trials, and the means of those trials were included in the analysis.

Spontaneous activity

Spontaneous movements of the mice were measured in a small, transparent cylinder 15.5 cm high and 12.7 cm in diameter (36,61–65). The cylinder was placed on a piece of glass with a mirror positioned at an angle beneath the cylinder to allow a clear view of movements along the ground and walls of the cylinder. Videotapes were viewed and rated in slow motion by an experimenter blind to mouse genotype. The number of rears, forelimb and hindlimb steps, and time spent grooming over a 3-min period were measured for each mouse.

Gait analysis

To measure gait, animals were trained to walk through a narrow alley leading into their home cage. Once trained, paper was placed along the alley floor and each animal's hindlimbs were brushed with non-toxic paint. Animals were then placed at the beginning of the alley. As they walked into their home cage they left their paw prints on the paper underneath (35,36,61,66–68). The stride length was determined by measuring the distance between hindlimb prints. Only strides made while continuously walking (no stopping) were included in the analysis. Stride lengths at the beginning and end of the alley were not counted since animals tend to make irregular steps at the beginning and typically stop and make smaller steps just before entering the cage. In addition, the range of stride lengths for each animal was measured by subtracting the shortest stride length from the longest stride length (69).

Nest building

Nest building, a natural mouse behavior was measured in *Atp13a2*$^{+/+}$ and *Atp13a2*$^{-/-}$ mice at 20–29 months of age. The behavior requires the use of orofacial and complex forelimb movements, where animals pull the nesting material apart with their forelimbs and teeth and then break down the material in their mouths and incorporate it into their bedding (36,70–73). Pre-weighed cotton was placed into the feeder of the cage in individually housed mice. Pulling the cotton from the feeder requires rearing up in addition to complex fine motor skills. Cotton use was monitored at 24 h by weighing the remaining cotton in the feeder.

Cognitive testing

Water-maze learning and memory, novel object and spatial recognition and locomotor/exploratory activity tests are described in detail in the Supplementary Material, Methods.

Quantitative RT–PCR array analyses

Total RNA was extracted from freshly dissected mouse brain tissues from 8- to 15-month-old mice using TRI Reagent® (Molecular Research Center). Prior to use in cDNA synthesis

reactions, RNAs were further purified to remove DNA and other contaminants by using an RNeasy® Mini kit (Qiagen). RNA concentration and purity were assessed spectrophotometrically using a NanoDrop ND-1000 (Thermo Scientific NanoDrop Products). RNA samples were reverse-transcribed using an RT^2 First-Strand cDNA kit (SABiosciences) and gene expression levels in *Atp13a2*$^{+/+}$ and *Atp13a2*$^{-/-}$ tissues were compared using Autophagy (PAMM-084) and Parkinson's (PAMM-124) RT^2 Profiler PCR arrays (SABiosciences) according to the manufacturer's procedures. Complete listings of the genes in each array are available at http://www.sabiosciences.com/ArrayList.php?pline=PCRArray. Thermocycling and data collection were carried out with a model 7300 Real-Time PCR system (Applied Biosystems) and data were analyzed by the $\Delta\Delta C_T$ method (74) using the Web-based RT^2 Profiler PCR Array Data Analysis tool (version 3.5, SABiosciences). For analyses of gene expression in the mouse striatum, the *Gusb*, *Hsp90ab1*, *Gapdh* and *Actb* transcripts were used as internal housekeeping controls. For analyses of expression in the SN, the *Hsp90ab1*, *Gapdh* and *Actb* transcripts were used.

Soluble and insoluble α-synuclein accumulation

To detect Triton and SDS soluble forms of α-synuclein, tau and huntingtin proteins, lysates from the frontal cortex, hippocampus and cerebellum of mutant and wild-type mice at 18–20 months of age were sequentially extracted as described previously (75). Frozen brains were homogenized in Triton X-100 solution with a homogenizer (Glas-Col), and subjected to four freeze-thaw cycles. Homogenates were then centrifuged at 100 000*g* for 30 min. After taking supernatants, the pellets were homogenized in Triton X-100 solution and centrifuged again. The second supernatants were mixed with the first one and used as Triton-soluble (T-sol) fractions. The pellets were resuspended with 2% SDS buffer, sonicated and boiled for 10 min. After centrifugation at 16 000*g* for 30 min, the supernatants were removed and used as SDS-soluble (SDS-sol) fractions. Thirty micrograms of protein was loaded on 4–12% Tris–glycine gels or 3–8% Tris–acetate gels. After separation, samples were transferred to PVDF membranes (Millipore), which were fixed in 0.4% PFA/TBS for 10 min, and then blocked in 5% milk/TBS with 0.1% Tween20 (TBS-T) for 1 h at RT. Membranes were incubated with α-synuclein antibody (202; Covance), tau antibody (A0024; Dako) or huntingtin antibody (5656; Cell Signaling) in TBS-T with 5% BSA at 4°C overnight. After washing 3 times with TBS-T, the membranes were incubated with secondary antibodies for 1 h at RT. The membranes were visualized using a LI-COR Odyssey infrared fluorescence scanner.

GCase enzyme activity assay

The mouse brain tissue was diluted 1:10 (w/v) in citrate-phosphate extraction buffer [150 mM citrate-phosphate buffer pH 5.4, 0.25% Triton X-100, protease inhibitor mix (Roche Diagnostics, Indianapolis, IN, USA)] and homogenized with a mechanical tissue homogenizer (Omni International, Kennesaw, GA, USA). The homogenate was sonicated for 2 × 10 s at 50% amplitude followed by centrifugation at 10 000*g* for 15 min at 4°C. The GCase enzyme activity assay was based on a previously described method (76). GCase or GAA activity was measured in assay buffer which consisted of citrate-phosphate buffer (pH 5.4) with 10 mM 4-methylumbelliferyl-β-D-glucopyranoside (4MU-β-glc) or 10 mM 4-methylumbelliferyl-α-D-glucopyranoside (4MU-α-glc), respectively. NaTC was not added to the buffer since this chemical is known to overactivate the GCase enzyme (77), which could skew read-out of the assay. Briefly, 5 µl of brain extract was added to wells of black 384-well plates (Greiner Bio-One, Inc, Monroe, NC, USA). On each plate, each sample was read in triplicate. For the GCase assay, conduritol-B-epoxide (CBE) triplicates were included for correction of GBA2 activity; 5 µl of 100 µM CBE was added followed by brief centrifugation and incubation at 37°C for 15 min at 600 rpm on a plate shaker. Assay buffer was added to each well to a total volume of 30 µl and incubated at 37°C for 1 h at 600 rpm. Thirty milliliters of stop solution (1 M glycine, pH 12.5) was added to each well and the fluorescence was measured using a Victor plate reader (Perkin-Elmer, Waltham, MA, USA), at 365 nm excitation and 440 nm emission. Enzyme activity was normalized to total protein amount.

Measurement of GCase protein levels in mouse brain extracts

A GCase-specific chemical probe (MDW933) was synthesized at the Imaging Probe Development Center (IPDC, NHLBI, NIH) as previously described (27). Total protein amount in each sample was determined by the Bradford assay according to the manufacturer's guidelines (Bio-Rad, Hercules, CA, USA). Ten micrograms of mouse brain tissue homogenate was incubated with 100 nM green fluorescent MDW933 probe in NaAc buffer (pH 5.0) for 90 min at 37°C followed by analysis on SDS–PAGE. As a control, we incubated 60 nM Cerezyme (Genzyme, Cambridge, MA, USA) with 100 nM MDW933 probe. Fluorescent signal in the gel was detected with a Typhoon Variable Mode Imager (Amersham Biosciences, Piscataway, NJ, USA) with λex at 488 nm and λem at 520 nm. ImageJ was used for densitometry analysis (version 1.44o; NIH, Bethesda, MD, USA).

Measurement of striatal dopamine content

Brains were removed from 20 to 29-month-old *Atp13a2*$^{+/+}$ and *Atp13a2*$^{-/-}$ mice ($n = 10$ for each genotype), and one hemisphere was flash frozen in liquid nitrogen for striatal DA measurements and the other was fixed in 4% paraformaldehyde for 20 h and then processed for stereology. Striatal DA levels were analyzed by the Neurochemistry Core Laboratory in the Center for Molecular Neuroscience at Vanderbilt University. Striatal punches were homogenized in 100–750 µl of 0.1 M trichloracetic acid (TCA), 10^{-2} M sodium acetate, 10^{-4} M EDTA, 5 ng/ml isoproterenol (as an internal standard) and 10.5% methanol (pH 3.8). Samples were centrifuged at 10 000*g* for 20 min, and the pellet and supernatant were stored separately at −80°C. Supernatant was thawed and spun for 20 min and then analyzed for biogenic amines using an HPLC assay utilizing an Antec Decade II (oxidation: 0.5) electrochemical detector at 33°C. Twenty microlitre samples were injected using a

Water 717+ autosampler onto a Phenomenex Nucleosil (5 μm, 100 Å) C18 HPLC column (150 × 4.60 mm). Biogenic amines were eluted with a mobile phase consisting of 89.5% 0.1 M TCA, 10^{-2} M sodium acetate, 10^{-4} M EDTA and 10.5% methanol (pH 3.8). Solvent was delivered at 0.6 ml/min using a Waters 515 HPLC pump. Using this HPLC solvent the following biogenic amines were eluted in the following order: noradrenaline, 3-methoxy-4-hydroxyphenylglycol, adrenaline, 3,4-dihydroxyphenylacetic acid (DOPAC), DA, 5-hydroxyindole acetic acid (5-HIAA), homovanillic acid (HVA), 5-hydroxytryptamine (serotonin, 5-HT) and 3-methoxytyramine. HPLC control and data acquisition were managed by the Millennium 32 software. Total protein concentration of the brain extracts was determined by the standard BCA Protein Assay (Pierce Chemical, Rockford, IL, USA).

Tyrosine hydroxylase immunostaining and stereology

After fixation (see above) brain hemispheres from 6 *Atp13a2*$^{+/+}$ mice and 6 *Atp13a2*$^{-/-}$ mice, ages 20–29 months were processed for stereology. TH immunostaining was performed by FD Neurotechnologies (Ellicott City, MD, USA). Serial cryostat sections (40 μm) were cut coronally through the cerebrum and the brain stem containing the striatum, the SN and the locus coeruleus, ∼1.94 to −5.88 mm from Bregma (78). TH immunohistochemistry was performed on sections from the SN (∼−2.30 to −4.16 mm from Bregma). After inactivating the endogenous peroxidase activity with hydrogen peroxidase, sections were incubated separately with avidin and biotin solutions (Vector Lab, Burlingame, CA, USA) to block non-specific binding of endogenous biotin, biotin-binding protein and lectins. Sections were then incubated free-floating in PBS-containing normal blocking serum, Triton X-100 and specific antibody for 3 days at 4°C. Subsequently, the immunoreaction product was visualized by the avidin–biotin complex method using a Vectastin elite ABC kit (Vector Lab., Burlingame, CA, USA) and 3′,3′-diaminobenzidine as a chromogen. After washing, all sections were mounted on gelatin-coated slides, counterstained with thionin, dehydrated in ethanol, cleared in xylene and coverslipped in Permount® (Fisher Scientific, Fair Lawn, NJ, USA).

The total number of TH-immunoreactive neurons in the SN and the total volume of SN were quantified using the optical fractionator method (79) and the Cavalieri-point counting method (80), as previously reported (81–83). These studies were carried out with assistance from a commercially available computerized stereology system (*Stereologer*) by trained personnel blind to group and genotype at a contract research organization (Stereology Resource Center, Chester, MD, USA).

Histology

Brains were isolated from 15- to 18-month-old mutant and wild-type mice. LFB-PAS staining was performed on paraffin sections as previously described (84). For autofluorescence, deparafinized and rehydrated sections were coverslipped with fluorescent mounting medium and viewed under a fluorescent microscope.

Statistical analysis

Challenging beam, spontaneous activity and gait data collected from *Atp13a2*$^{+/+}$ and *Atp13a2*$^{-/-}$ mice at 5–12 months of age were analyzed using Student's *t*-test or the Mann–Whitney *U* test depending on whether the data maintained homogeneity of variance. Similarly, beam, activity, gait and nestbuilding data collected in a separate cohort of mice at 20–29 months of age were analyzed using Student's *t*-test or the Mann–Whitney *U* test. Beam data at 20–29 months were also analyzed by trial. Here, a 2 × 5 mixed design ANOVA was used to compare scores between genotypes across each of the five trials. *Post hoc* analysis was done using Fisher's LSD. All analyses were conducted with the GB-STAT software (Dynamic Microsystems, Inc., Silver Spring, MD, 2000) for Macintosh. The level of significance was set at $P < 0.05$.

SUPPLEMENTARY MATERIAL

Supplementary Material is available at *HMG* online.

ACKNOWLEDGEMENTS

We thank the Gene Targeted Mouse Service Core of the University of Cincinnati College of Medicine for design and construction of the targeting vector and generation of mice heterozygous for *Atp13a2*. Additional thanks to Abbey Bailes, Christina Basinger and Kelsey Carnahan of the Schultheis lab for their help with maintenance of the *Atp13a2* mouse colony. We also thank Dr Gary Griffiths and Dr Zhen-Dan Shi (IPDC, NHLBI, NIH) for synthesis of the MDW933 probe.

Conflict of Interest statement. None declared.

FUNDING

This work was supported by the National Institutes of Health (NS070268 to P.J.S., GM103436 to P.J.S. and M.E.B., DK050594 and HL061974 to G.E.S., NS077022 to S.M.F., MH094955 to M.E.B., NS076054 to D.K.); the UF CTRND and Department of Neuroscience; the UC Gardner Family Center for Parkinson's Disease and Movement Disorders and the Intramural Research program of the National Human Genome Research Institute at the National Institutes of Health, Bethesda, MD, USA.

REFERENCES

1. Schultheis, P.J., Hagen, T.T., O'Toole, K.K., Tachibana, A., Burke, C.R., McGill, D.L., Okunade, G.W. and Shull, G.E. (2004) Characterization of the P5 subfamily of P-type transport ATPases in mice. *Biochem. Biophys. Res. Comm.*, **323**, 731–738.
2. Sørensen, D.M., Buch-Pedersen, M.J. and Palmgren, M.G. (2010) Structural divergence between the two subgroups of P5 ATPases. *Biochim. Biophys. Acta*, **1797**, 846–855.
3. Ramirez, A., Heimbach, A., Grundemann, J., Stiller, B., Hampshire, D., Cid, L.P., Goebel, I., Mubaidin, A.F., Wriekat, A.-L., Roeper, J. *et al.* (2006) Hereditary parkinsonism with dementia is caused by mutations in *ATP13A2*, encoding a lysosomal type 5 P-type ATPase. *Nature Genet.*, **38**, 1184–1191.
4. Farias, F.H.G., Zeng, R., Johnson, G.S., Wininger, F.A., Taylor, J.F., Schnabel, R.D., McKay, S.D., Sanders, D.N., Lohi, H., Seppala, E.H.

et al. (2011) A truncating mutation in *ATP13A2* is responsible for adult-onset neuronal ceroid lipofuscinosis in Tibetan terriers. *Neurobiol. Dis.*, **42**, 468–474.
5. Wohlke, A., Philipp, U., Bock, P., Beineke, A., Lichtner, P., Meitinger, T. and Distl, O. (2001) A one base pair deletion in the canine *ATP13A2* gene causes exon skipping and Late-onset Neuronal Ceroid Lipofusccinosis in the Tibetan Terrier. *PLoS Genet.*, **7**, e1002304 doi: 10.1371/journal.pgen1002304
6. Bras, J., Verloes, A., Schneider, S.A., Mole, S.E. and Guerreiro, R.J. (2012) Mutation of the parkinsonism gene *ATP13A2* causes neuronal ceroid-lipfuscinosis. *Hum. Mol. Gen.*, **21**, 2646–2650.
7. Najim Al-Din, A.S., Wriekat, A., Mubaidin, A., Dasouki, M. and Hiari, M. (1994) Pallido-pyramidal degeneration, supranuclear upgaze paresis and dementia: Kufor-Rakeb syndrome. *Acta Neurol. Scand.*, **89**, 347–352.
8. Williams, D.R., Hadeed, A., Al-Din, A.S., Wreikat, A.L. and Lees, A.J. (2005) Kufor Rakeb disease: autosomal recessive, levodopa-responsive parkinsonism with pyramidal degeneration, supranuclear gaze palsy, and dementia. *Mov. Disord.*, **20**, 1264–1271.
9. Lees, A.J. and Singleton, A.B. (2007) Clinical heterogeneity of *ATP13A2* linked disease (Kufor-Rakeb) justifies a PARK designation. *Neurology*, **68**, 1553–1554.
10. Jalanko, A. and Braulke, T. (2009) Neuronal ceroid lipfuscinoses. *Biochem. Biophys. Acta*, **1793**, 697–709.
11. Tome, F.M., Brunet, P., Fardeau, M., Hentati, F. and Reix, J. (1985) Familial disorder of the central and peripheral nervous systems with particular cytoplasmic lamellated inclusions in peripheral nerves, muscle satellite cells, and blood capillaries. *Acta Neuropathol.*, **68**, 209–217.
12. De Volder, A.G., Cirelli, S., de Barsy, T., Brucher, J.M., Bol, A., Michel, C. and Goffinet, A.M. (1990) Neuronal ceroid-lipofuscinosis: preferential metabolic alterations in thalamus and posterior association cortex demonstrated by PET. *J. Neurol. Neurosurg. Psychiatry*, **53**, 1063–1067.
13. Schmidt, K., Wolfe, D.M., Stiller, B. and Pearce, D.A. (2009) Cd^{2+}, Mn^{2+}, Ni^{2+}, and Se^{2+} toxicity to Saccharomyces cerevisiae lacking YPK9p the orthologue of human *ATP13A2*. *Biochem. Biophys. Res. Comm.*, **383**, 198–202.
14. Gitler, A.D., Chesi, A., Geddie, M.L., Strathearn, K.E., Hamamichi, S., Hill, K.J., Caldwell, K.A., Caldwell, G.A., Cooper, A.A., Rochet, J.C. *et al.* (2009) Alpha-synuclein is part of a diverse and highly conserved interaction network that includes PARK9 and manganese toxicity. *Nat. Genet.*, **41**, 308–315.
15. Burton, N.C. and Guilarte, T.R. (2009) Manganese neurotoxicity: lessons learned from longitudinal studies in nonhuman primates. *Environ. Health. Perspect.*, **117**, 325–332.
16. Usenovic, M., Tresse, E., Mazzulli, J.R., Taylor, J.P. and Krainc, D. (2012) Deficiency of ATP13A2 leads to lysosomal dysfunction, α-synuclein accumulation, and neurotoxicity. *J. Neurosci.*, **32**, 4240–4246.
17. Polymeropoulos, M.H., Lavedan, C., Leroy, E., Ide, S.E., Dehejia, A., Dutra, A., Pike, B., Root, H., Rubenstein, J., Boyer, R. *et al.* (1997) Mutation in the α-synuclein gene identified in families with Parkinson's disease. *Science*, **276**, 2045–2047.
18. Spillantini, M.G., Crowther, R.A., Jakes, R., Hasegawa, M. and Goedert, M. (1998) α-Synuclein in filamentous inclusions of Lewy bodies from Parkinson's disease and dementia with Lewy bodies. *Proc. Natl Acad. Sci. USA*, **95**, 6469–6473.
19. Luk, K.C., Kehm, V., Carroll, J., Zhang, B., O'Brien, P., Trojanowski, J.Q. and Lee, V.M. (2012) Pathological α-synuclein transmission initiates Parkinson-like neurodegeneration in nontransgenic mice. *Science*, **338**, 949–953.
20. Dehay, B., Ramirez, A., Martinez-Vicente, M., Perier, C., Canron, M.H., Doudnikoff, E., Vital, A., Vila, M., Klein, C. and Bezard, E. (2012) Loss of P-type ATPase ATP13A2/PARK9 function induces general lysosome deficiency and leads to Parkinson disease neurodegeneration. *Proc. Natl Acad. Sci. USA*, **109**, 9611–9616.
21. Haltia, M. (2006) The neuronal ceroid-liposuscinoses: from past to present. *Biochim. Biophys. Acta*, **1762**, 850–856.
22. Balducci, C., Pierguidi, L., Persichetti, E., Parnetti, L., Sbaragli, M., Tassi, C., Orlacchio, A., Calabresi, P., Beccari, T. and Rossi, A. (2007) Lysosomal hydrolases in cerebrospinal fluid from subjects with Parkinson's disease. *Mov. Disord.*, **22**, 1481–1484.
23. Gegg, M.E., Burke, D., Heales, S.J., Cooper, J.M., Hardy, J., Wood, N.W. and Schapira, A.H. (2012) Glucocerebrosidase deficiency in substantia nigra of Parkinson disease brains. *Ann. Neurol.*, **72**, 455–463.
24. Parnetti, L., Balducci, C., Pierguidi, L., De Carlo, C., Peducci, M., D'Amore, C., Padiglioni, C., Mastrocola, S., Persichetti, E., Paciotti, S. *et al.* (2009) Cerebrospinal fluid beta-glucocerebrosidase activity is reduced in Dementia with Lewy Bodies. *Neurobiol. Dis.*, **34**, 484–486.
25. Sardi, S.P., Clarke, J., Viel, C., Chan, M., Tamsett, T.J., Treleaven, C.M., Bu, J., Sweet, L., Passini, M.A., Dodge, J.C. *et al.* (2013) Augmenting CNS glucocerebrosidase activity as a therapeutic strategy for parkinsonism and other Gaucher-related synucleinopathies. *Proc. Natl Acad. Sci. USA.* (Epub ahead of print).
26. Raben, N., Wong, A., Ralston, E. and Myerowitz, R. (2012) Autophagy and mitochondria in Pompe disease: nothing is so new as what has long been forgotten. *Am. J. Med. Genet. C Semin. Med. Genet.*, **160**, 13–21.
27. Witte, M.D., Kallemeijn, W.W., Aten, J., Li, K.Y., Strijland, A., Donker-Koopman, W.E., van den Nieuwendijk, A.M., Bleijlevens, B., Kramer, G., Florea, B.I. *et al.* (2010) Ultrasensitive *in situ* visualization of active glucocerebrosidase molecules. *Nat. Chem. Biol.*, **6**, 907–913.
28. Park, J.S., Mehta, P., Cooper, A.A., Veivers, D., Heimbach, A., Stiller, B., Kubisch, C., Fung, V.S., Krainc, D., Mackay-Sim, A. *et al.* (2011) Pathogenic effects of novel mutations in the P-type ATPase ATP13A2 (PARK9) causing Kufor-Rakeb syndrome, a form of early-onset parkinsonism. *Hum. Mutat.*, **32**, 956–64.
29. Ugolino, J., Fang, S., Kubisch, C. and Monteiro, M.J. (2011) Mutant Atp13a2 proteins involved in parkinsonism are degraded by ER-associated degradation and sensitize cells to ER-stress induced cell death. *Hum. Mol. Genet.*, **20**, 3565–3577.
30. Eiberg, H., Hansen, L., Korbo, L., Nielsen, I.M., Svenstrup, K., Bech, S., Pinborg, L.H., Friberg, L., Hjermind, L.E., Olsen, O.R. *et al.* (2012) Novel mutation in ATP13A2 widens the spectrum of Kufor-R*a*keb syndrome (PARK9). *Clin. Genet.*, **82**, 256–263.
31. Hampshire, D.J., Roberts, E., Crow, Y., Bond, J., Mubaidin, A., Wriekat, A.L., Al-Din, A. and Woods, C.G. (2001) Kufor-Rakeb syndrome, pallido-pyramidal degeneration with supranuclear upgaze paresis and dementia, maps to 1p36. *J. Med. Genet.*, **38**, 680–682.
32. Behrens, M.I., Brüggemann, N., Chana, P., Venegas, P., Kägi, M., Parrao, T., Orellana, P., Garrido, C., Rojas, C.V., Hauke, J. *et al.* (2010) Clinical spectrum of Kufor-Rakeb syndrome in the Chilean kindred with ATP13A2 mutations. *Mov. Disord.*, **25**, 1929–1937.
33. Riis, R.C., Cummings, J.F., Loew, E.R. and de Lahunta, A. (1992) Tibetan terrier model of canine ceroid lipofuscinosis. *Am. J. Med. Genet.*, **42**, 615–621.
34. Katz, M.L., Shibuya, H. and Johnson, G.S. (2001) Animal models for the ceroid lipofuscinoses. *Adv. Genet.*, **45**, 183–203.
35. Barlow, C., Hirotsune, S., Paylor, R., Liyanage, M., Eckhaus, M., Collins, F., Shiloh, Y., Crawley, J.N., Ried, T., Tagle, D. *et al.* (1996) Atm-deficient mice: a paradigm of ataxia telangiectasia. *Cell*, **86**, 159–171.
36. Fleming, S.M., Salcedo, J., Fernagut, P.O., Rockenstein, E., Masliah, E., Levine, M.S. and Chesselet, M.F. (2004) Early and progressive sensorimotor anomalies in mice overexpressing wild-type human alpha-synuclein. *J. Neurosci.*, **24**, 9434–9440.
37. Glajch, K.E., Fleming, S.M., Surmeier, D.J. and Osten, P. (2012) Sensorimotor assessment of the unilateral 6-hydroxydopamine mouse model of Parkinson's disease. *Behav. Brain Res.*, **230**, 309–316.
38. Reliene, R., Fleming, S.M., Chesselet, M.F. and Schiestl, R.H. (2008) Effects of antioxidants oncancer prevention and neuromotor performance in Atm deficient mice. *Food Chem. Toxicol.*, **46**, 1371–1377.
39. Henriksen, E.J., Colgin, L.L., Barnes, C.A., Witter, M.P., Moser, M.B. and Moser, E.I. (2010) Spatial representation along the proximodistal axis of CA1. *Neuron*, **68**, 127–137.
40. Hartley, M., Taylor, N. and Taylor, J. (2005) Subfield variations in hippocampal processing-components of a spatial navigation system. *Neural. Netw.*, **18**, 611–619.
41. Navarro, P., Guerrero, R., Gallego, E., Avila, J., Luquin, R., Garcia Ruiz, P.J. and Sanchez, M.P. (2008) Motor alterations are reduced in mice lacking the PARK2 gene in the presence of a human FTDP-17 mutant form of four-repeat tau. *J. Neurol. Sci.*, **275**, 139–144.
42. Schneider, S.A., Paisan-Ruiz, C., Quinn, N.P., Lees, A.J., Houlden, H., Hardy, J. and Bhatia, K.P. (2010) *ATP13A2* mutations (PARK9) cause neurodegeneration with brain iron accumulation. Mov. Disord., **25**, 979–984.
43. Brüggemann, N., Hagenah, J., Reetz, K., Schmidt, A., Kasten, M., Buchmann, I., Eckerle, S., Bähre, M., Münchau, A., Djarmati, A. *et al.* (2010) Recessively inherited parkinsonism: effect of *ATP13A2* mutations on the clinical and neuroimaging phenotype. *Arch. Neurol.*, **67**, 1357–1363.

44. Munnel, J.F. and Getty, R. (1968) Rate of accumulation of cardiac lipofuscin in the aging canine. *J. Gerontol.*, **23**, 154–158.
45. Nakano, M. and Gotoh, S. (1992) Accumulation of cardiac lipofuscin depends on metabolic rate of mammals. *J. Gerontol.*, **47**, B126–B129.
46. Sheehy, M.R., Greenwood, J.G. and Fielder, D.R. (1995) Lipofuscin as a record of rate of living in an aquatic poikilotherm. *J. Gerontol.*, **50**, B327–B336.
47. Neufeld, E.F. (1991) Lysosomal storage diseases. *Annu. Rev. Biochem.*, **60**, 257–280.
48. Cookson, M.R. (2009) α-Synuclein and neuronal cell death. *Mol. Degeneration*, **4**, 9 doi:10.1186/1750–1326–4–9.
49. Auluck, P.K., Caraveo, G. and Lindquist, S. (2010) α synuclein: membrane interactions and toxicity in Parkinson's disease. *Annu. Rev. Cell Dev. Biol.*, **26**, 211–233.
50. Mazzulli, J.R., Xu, Y.H., Sun, Y., Knight, A.L., McLean, P.J., Caldwell, G.A., Sidransky, E., Grabowski, G.A. and Krainc, D. (2011) Gaucher disease glucocerebrosidase and α-synuclein form a bidirectional pathogenic loop in synucleinopathies. *Cell*, **146**, 37–52.
51. Sidransky, E., Nalls, M.A., Aasly, J.O., Aharon-Peretz, J., Annesi, G., Barbosa, E.R., Bar-Shira, A., Berg, D., Bras, J., Brice, A. *et al.* (2009) Multicenter analysis of glucocerebrosidase mutations in Parkinson's disease. *N.Engl. J. Med.*, **361**, 1651–1661.
52. Cuervo, A.M., Stefanis, L., Fredenburg, R., Lansbury, P.T. and Sulzer, D. (2004) Impaired degradation of mutant α-synuclein by chaperone-mediated autophagy. *Science*, **305**, 1292–1295.
53. Jankovic, J., Chen, S. and Le, W.D. (2005) The role of *Nurr1* in the development of dopaminergic neurons and Parkinson's disease. *Prog. Neurobiol.*, **77**, 128–138.
54. Howells, D.W., Porritt, M.J., Wong, J.Y., Batchelor, P.E., Kalnins, R., Hughes, A.J. and Donnan, G.A. (2000) Reduced BDNF mRNA expression in the Parkinson's disease substantia nigra. *Exp. Neurol.*, **166**, 127–135.
55. Cronin, S.R., Rao, R. and Hampton, R.Y. (2002) Cod1p/Spf1p is a P-type ATPase involved in ER function and Ca^{2+} homeostasis. *J. Cell Biol.*, **157**, 1017–1028.
56. Covy, J.P., Waxman, E.A. and Giasson, B.I. (2012) Characterization of cellular protective effects of ATP13A2/PARK9 expression and alterations resulting from pathogenic mutants. *J. Neurosci. Res.*, **90**, 2306–2316.
57. Bras, J., Singleton, A., Cookson, M.R. and Hardy, J. (2008) Emerging pathways in genetic Parkinson's disease: potential role of ceramide metabolism in Lewy body disease. *FEBS J.*, **275**, 5767–5773.
58. Folmer, D.E., Elferink, R.P. and Paulusma, C.C. (2009) P_4 ATPases—lipid flippases and their role in disease. *Biochim. Biophys. Acta.*, **1791**, 628–35.
59. Cronin, S.R., Khoury, A., Ferry, D.K. and Hampton, R.Y. (2000) Regulation of HMG-CoA reductase degradation requires the P-type ATPase Cod1p/Spflp. *J. Cell Biol.*, **148**, 915–924.
60. Schultheis, P.J., Clarke, L.L., Meneton, P., Harline, M., Boivin, G.P., Stemmermann, G., Duffy, J.J., Doetschman, T., Miller, M.L. and Shull, G.E. (1998) Targeted disruption of the murine Na^+/H^+ exchanger isoform 2 gene causes reduced viability of gastric parietal cells and loss of net acid secretion. *J. Clin. Invest.*, **101**, 1243–1253.
61. Fleming, S.M., Salcedo, J., Hutson, C.B., Rockenstein, E., Masliah, E., Levine, M.S. and Chesselet, M.F. (2006) Behavioral effects of dopaminergic agonists in transgenic mice overexpressing human wildtype alpha-synuclein. *Neuroscience*, **142**, 1245–1253.
62. Fleming, S.M., Mulligan, C.K., Richter, F., Mortazavi, F., Lemesre, V., Frias, C., Zhu, C., Stewart, A., Gozes, I., Morimoto, B. *et al.* (2011) A pilot trial of the microtubule-interacting peptide (NAP) in mice overexpressing alpha-synuclein shows improvement in motor function and reduction of alpha-synuclein inclusions. *Mol. Cell Neurosci.*, **46**, 597–606.
63. Goldberg, M.S., Fleming, S.M., Palacino, J.J., Cepeda, C., Lam, H.A., Bhatnagar, A., Meloni, E.G., Wu, N., Ackerson, L.C., Klapstein, G.J. *et al.* (2003) Parkin-deficient mice exhibit nigrostriatal deficits but not loss of dopaminergic neurons. *J. Biol. Chem.*, **278**, 43628–43635.
64. Hwang, D.Y., Fleming, S.M., Ardayfio, P., Moran-Gates, T., Kim, H., Tarazi, F.I., Chesselet, M.F. and Kim, K.S. (2005) 3,4-dihydroxyphenylalanine reverses the motor deficits in Pitx3-deficient aphakia mice: behavioral characterization of a novel genetic model of Parkinson's disease. *J. Neurosci.*, **25**, 2132–2137.
65. Lu, X.H., Fleming, S.M., Meurers, B., Ackerson, L.C., Mortazavi, F., Lo, V., Hernandez, D., Sulzer, D., Jackson, G.R., Maidment, N.T. *et al.* (2009) Bacterial artificial chromosome transgenic mice expressing a truncated mutant parkin exhibit age-dependent hypokinetic motor deficits, dopaminergic neuron degeneration, and accumulation of proteinase K-resistant alpha-synuclein. *J. Neurosci.*, **29**, 1962–1976.
66. Schallert, T., Whishaw, I.Q., Ramirez, V.D. and Teitelbaum, P. (1978) Compulsive, abnormal walking caused by anticholinergics in akinetic, 6-hydroxydopamine-treated rats. *Science*, **199**, 1461–1463.
67. Fernagut, P.O., Diguet, E., Labattu, B. and Tison, F. (2002) A simple method to measure stride length as an index of nigrostriatal dysfunction in mice. *J. Neurosci. Methods*, **113**, 123–130.
68. Tillerson, J.L., Caudle, W.M., Reverón, M.E. and Miller, G.W. (2002) Detection of behavioral impairments correlated to neurochemical deficits in mice treated with moderate doses of 1-methyl-4-phenyl-1,2,3,6-tetrahydropyridine. *Exp. Neurol.*, **178**, 80–90.
69. Dunnett, S.B. (2003) Assessment of motor impairments in transgenic mice. In Crawley, J.N. (ed.), *Mouse Behavioral Phenotyping*. Society for Neuroscience, Washington, DC, pp. 1–12.
70. Upchurch, M. and Schallert, T. (1983) A behavior analysis of the offspring of "haloperidol-sensitive" and "haloperidol-resistant" gerbils. *Behav. Neural. Biol.*, **39**, 221–228.
71. Sedelis, M., Hofele, K., Auburger, G.W., Morgan, S., Huston, J.P. and Schwarting, R.K. (2000) MPTP susceptibility in the mouse: behavioral, neurochemical, and histological analysis of gender and strain differences. *Behav. Genet.*, **30**, 171–182.
72. Hofele, K., Sedelis, M., Auburger, G.W., Morgan, S., Huston, J.P. and Schwarting, R.K. (2001) Evidence for a dissociation between MPTP toxicity and tyrosinase activity based on congenic mouse strain susceptibility. *Exp. Neurol.*, **168**, 116–122.
73. Szczypka, M.S., Kwok, K., Brot, M.D., Marck, B.T., Matsumoto, A.M., Donahue, B.A. and Palmiter, R.D. (2001) Dopamine production in the caudate putamen restores feeding in dopamine-deficient mice. *Neuron*, **30**, 819–828.
74. Livak, K.J. and Schmittgen, T.D. (2001) Analysis of relative gene expression data using real-time quantitative PCR and the $2_T^{-\Delta\Delta C}$ method. *Methods*, **25**, 402–408.
75. Mazzulli, J.R., Mishizen, A.J., Giasson, B.I., Lynch, D.R., Thomas, S.A., Nakashima, A., Nagatsu, T., Ota, A. and Ischiropoulos, H. (2006) Cytosolic catechols inhibit alpha-synuclein aggregation and facilitate the formation of intracellular soluble oligomeric intermediates. *J. Neurosci.*, **26**, 10068–10078.
76. Marshall, J., McEachern, K.A., Kyros, J.A., Nietupski, J.B., Budzinski, T., Ziegler, R.J., Yew, N.S., Sullivan, J., Scaria, A., van Rooijen, N. *et al.* (2002) Demonstration of feasibility of *in vivo* gene therapy for Gaucher disease using a chemically induced mouse model. *Mol. Ther.*, **6**, 179–189.
77. Goldin, E., Zheng, W., Motabar, O., Southall, N., Choi, J.H., Marugan, J., Austin, C.P. and Sidransky, E. (2012) High throughput screening for small molecule therapy for Gaucher disease using patient tissue as the source of mutant glucocerebrosidase. *PLoS One*, **7**, e29861.
78. Paxinos, G. and Franklin, K.B.J. (2004) *The Mouse Brain in Stereotaxic Coordinates*, 2nd edn. Elsevier Academic Press, San Diego, CA.
79. West, M.J., Slomianka, L. and Gundersen, H.J. (1991) Unbiased stereological estimation of the total number of neurons in the subdivisions of the rat hippocampus using the optical fractionator. *Anat. Rec.*, **231**, 482–497.
80. Gundersen, H.J.G., Jensen, E.B.V., Kieu, K. and Nielsen, J. (1999) The efficiency of systematic sampling in stereology–reconsidered. *J. Microsc.*, **193**, 199–211.
81. Manaye, K.F., Mouton, P.R., Xu, G., Drew, A., Lei, D.L., Sharma, Y., Rebeck, G.W. and Turner, S. (2013) Age-related loss of noradrenergic neurons in the brains of triple transgenic mice. *Age*, **35**, 139–147.
82. Mouton, P.R., Kelley-Bell, B., Tweedie, D., Spangler, E.L., Perez, E., Carlson, O.D., Short, R.G., Decabo, R., Chang, J., Ingram, D.K. *et al.* (2012) Effects of age and LPS-mediated inflammation on central catecholaminergic neuron number in B6 mice. *Neurobiol. Aging*, **423**, 27–36.
83. Mouton, P.R. (2011) *Unbiased Stereology: A Concise Guide*. The Johns Hopkins University Press, Baltimore, MD.
84. Ahmed, Z., Sheng, H., Xu, Y.F., Lin, W.L., Innes, A.E., Gass, J., Yu, X., Wuertzer, C.A., Hou, H., Chiba, S. *et al.* (2010) Accelerated lipofuscinosis and ubiquitination in granulin knockout mice suggest a role for progranulin in successful aging. *Am. J. Pathol.*, **177**, 311–324.